THE ASTROPHYSICAL JOURNAL, 522:357–377, 1999 September 1

INFRARED SPACE OBSERVATORY WITH THE OBSERVATIONS OF SOLID CARBON DIOXIDE IN MOLECULAR CLOUDS[1]

P. A. GERAKINES,[2,3] D. C. B. WHITTET,[2] P. EHRENFREUND,[4] A. C. A. BOOGERT,[5] A. G. G. M. TIELENS,[5,6] W. A. SCHUTTE,[4] J. E. CHIAR,[6] E. F. VAN DISHOECK,[4] T. PRUSTI,[7] F. P. HELMICH,[4,8] AND TH. DE GRAAUW[5,9]

Received 1998 September 11; accepted 1999 April 14

ABSTRACT

Spectra of interstellar CO_2 ice absorption features at a resolving power of $\lambda/\Delta\lambda \approx 1500$–$2000$ are presented for 14 lines of sight. The observations were made with the Short-Wavelength Spectrometer (SWS) of the *Infrared Space Observatory* (*ISO*). Spectral coverage includes the primary stretching mode of CO_2 near 4.27 μm in all sources; the bending mode near 15.2 μm is also detected in 12 of them. The selected sources include massive protostars (Elias 29 [in ρ Oph], GL 490, GL 2136, GL 2591, GL 4176, NGC 7538 IRS 1, NGC 7538 IRS 9, S140, W3 IRS 5, and W33 A), sources associated with the Galactic Center (Sgr A*, GCS 3 I, and GCS 4), and a background star behind a quiescent dark cloud in Taurus (Elias 16); they thus probe a diverse range of environments. Column densities of interstellar CO_2 ice relative to H_2O ice fall in the range 10%–23%: this ratio displays remarkably little variation for such a physically diverse sample. Comparison of the observed profiles with laboratory data for CO_2-bearing ice mixtures indicates that CO_2 generally exists in at least two phases, one polar (H_2O dominant) and one nonpolar (CO_2 dominant). The observed CO_2 profiles may also be reproduced when the nonpolar components are replaced with thermally annealed ices. Formation and evolutionary scenarios for CO_2 and implications for grain mantle chemistry are discussed. Our results support the conclusion that thermal annealing, rather than energetic processing due to UV photons or cosmic rays, dominates the evolution of CO_2-bearing ices.

Subject headings: dust, extinction — infrared: ISM: lines and bands — ISM: molecules — stars: pre–main-sequence

1. INTRODUCTION

The evolution of carbonaceous materials in the interstellar medium (ISM) is a key problem in astrophysics, with ramifications as far-reaching as the origins of life on Earth. To date, nearly 100 carbon-bearing species are known to exist in the gas phase of the ISM, most abundantly in the form of carbon monoxide, CO (see reviews by Snyder 1997; van Dishoeck & Blake 1998). Of these species, a handful have been detected in the solid state as constituents of icy grain mantles through infrared (IR) spectroscopy. Carbonaceous components of icy grain mantles detected to date include CO (Lacy et al. 1984), methane (CH_4; Boogert et al. 1996, 1998; Whittet et al. 1996; Lutz et al. 1996; d'Hendecourt et al. 1996), methanol (CH_3OH; Grim et al. 1991; Schutte, Tielens, & Sandford 1991; Skinner et al. 1992; Allamandola et al. 1992), "XCN" (a molecule or ion containing the CN group; Lacy et al. 1984; Tegler et al. 1995; Schutte & Greenberg 1997), and formaldehyde (H_2CO; tentative detection; Schutte et al. 1996a). Simple hydrocarbons may also be present (Brooke et al. 1996b; Chiar, Adamson, & Whittet 1996).

Before the launch of the *Infrared Space Observatory* (*ISO*), high-resolution spectroscopy in the mid-IR was limited to molecules with transitions in spectral regions free of significant atmospheric absorption. A full inventory of interstellar ices accessible to IR observation is now possible with *ISO*, and one of the early highlights in reaching this goal has been CO_2 (e.g., de Graauw et al. 1996b; Gürtler et al. 1996; d'Hendecourt et al. 1996; Lutz et al. 1996; Whittet et al. 1998). Here we present an analysis of high-resolution solid CO_2 observations ($\lambda/\Delta\lambda \approx 1500$–$2000$) toward a large variety of sources.

Dust grains inside quiescent, dense molecular clouds are shielded from the interstellar radiation field and may reach temperatures as low as 8–10 K in the absence of any internal heating sources (see, e.g., Pratap et al. 1997). Particles at these temperatures readily accrete species from the gas phase because of high sticking efficiencies and lack of efficient desorption mechanisms (see, e.g., Tielens & Allamandola 1987). Where the fraction of hydrogen in atomic form is substantial ($\sim$0.01%–1%), as in the outer regions of dense molecular clouds (e.g., Savage et al. 1977), models such as those by Tielens & Hagen (1982) and d'Hendecourt, Allamandola, & Greenberg (1985) predict that accreting atoms will form fully hydrogenated molecules via surface reactions with H (to produce mostly H_2O, CH_4, and NH_3). In denser regions, molecules that are abundant in the gas phase (e.g., CO, N_2, and O_2) will accrete directly onto the dust.

[1] Based on observations with the *Infrared Space Observatory*, an ESA project with instruments funded by ESA Member States (especially the PI countries: France, Germany, the Netherlands, and the United Kingdom) and with the participation of ISAS and NASA.

[2] Department of Physics, Applied Physics, and Astronomy, Rensselaer Polytechnic Institute, Troy, NY 12180.

[3] Present address: Code 691, NASA/Goddard Space Flight Center, Greenbelt, MD 20771.

[4] Leiden Observatory, P.O. Box 9513, 2300 RA Leiden, Netherlands.

[5] Kapteyn Astronomical Institute, P.O. Box 800, 9700 AV Groningen, Netherlands.

[6] NASA/Ames Research Center, Mail Stop 245-3, Moffett Field, CA 94035.

[7] *Infrared Space Observatory* Science Operations Center, Astrophysics Division, European Space Agency, Villafranca del Castillo, P.O. Box 50727, 28080 Madrid, Spain.

[8] Stichting Ruimte Onderzoek Nederland, Sorbonnelaan 2, 3584 CA Utrecht, Netherlands.

[9] Stichting Ruimte Onderzoek Nederland, P.O. Box 800, 9700 AV Groningen, Netherlands.

Carbon dioxide has several possible formation mechanisms in the ISM. While formation rates for CO_2 are low in the gas phase (Herbst & Leung 1989; Millar et al. 1991), laboratory experiments show that CO_2 is formed with extreme efficiency in irradiation experiments involving solid H_2O and CO (see, e.g., d'Hendecourt et al. 1985; Sandford & Allamandola 1990; Moore, Khanna, & Donn 1991). Thus, large amounts of CO_2 are predicted near luminous protostars with strong ultraviolet (UV) fields. Computational models that include grain surface chemistry (Tielens & Hagen 1982; d'Hendecourt et al. 1985; Hasegawa & Herbst 1993; Shalabiea & Greenberg 1994) also predict that CO_2 should be present in interstellar icy grain mantles, where the abundance of CO_2 produced is strongly dependent on whether the grain-surface oxidation of CO is possible. The laboratory results of Grim & d'Hendecourt (1986) indicate that this reaction may have an activation energy of 10–30 K, but such a barrier may be easily overcome in the ISM given the long timescales for diffusion-limited grain surface reactions (accretion rate ~ 1 species per day; Tielens & Whittet 1997). Moreover, the observation of abundant CO_2 in the quiescent ISM toward Elias 16 strongly suggests that processing of mantle ices due to embedded sources of radiation is not required to produce interstellar CO_2 (Whittet et al. 1998).

Infrared spectra of CO_2-bearing ices have been well studied in the laboratory in an astrophysical context by Sandford & Allamandola (1990), Gerakines et al. (1995), and Ehrenfreund et al. (1997). CO_2 has four observable absorptions in the mid-IR (two combination modes, one stretching mode, and one bending mode), the strongest of which is due to its asymmetric stretching fundamental vibration (ν_3) at 4.27 μm (2342 cm^{-1}): its strength is $A = 7.6 \times 10^{-17}$ cm molecule^{-1}, which may be compared with the values for the H_2O and CO stretching modes, $A = 2.0 \times 10^{-16}$ and 1.1×10^{-17} cm molecule^{-1}, respectively (Gerakines et al. 1995). This transition is strong enough to be observable even when the C atom is replaced by its isotope ^{13}C (terrestrially, 89 times less abundant than ^{12}C). The asymmetric stretching mode of $^{13}CO_2$ is located at 4.38 μm (2283 cm^{-1}). The symmetric stretching mode (ν_1) of CO_2 at 7.2 μm (1385 cm^{-1}) is normally unobservable since it produces no change in the molecule's dipole moment. The bending mode (ν_2) absorbs at a wavelength of 15.2 μm (660 cm^{-1}) and is 7 times weaker than the asymmetric stretching mode ($A = 1.1 \times 10^{-17}$ cm molecule^{-1}; Gerakines et al. 1995). The $\nu_1 + \nu_3$ and $2\nu_2 + \nu_3$ combination modes, located at 2.697 and 2.778 μm (3708 and 3600 cm^{-1}), are, respectively, 54 and 170 times weaker than the stretching mode.

The sensitivity of CO_2 infrared features to ice composition and temperature makes them ideal probes of interstellar cloud parameters. CO_2 is less volatile than CO and may exist in solid form up to temperatures of 50–90 K, depending on the ice in which it resides. It could therefore provide information on carbon chemistry in a wider range of environments than CO, which will sublime almost completely at temperatures above 30 K (although a small amount may exist at higher temperatures when trapped in some ice mixtures). The profiles of CO_2 features in polar ice mixtures (dominated by H_2O or CH_3OH) are dramatically different from those of CO_2 in nonpolar environments (dominated by molecules such as CO, O_2, or CO_2 itself) and thereby trace the chemical composition of interstellar ices (Sandford & Allamandola 1990; Ehrenfreund et al. 1997). Temperature history is also preserved in the structure of the 15.2 μm CO_2 bending mode, whose profile contains a complicated substructure when annealed (Ehrenfreund et al. 1999).

In this paper, we present an analysis of high-resolution spectroscopy ($\lambda/\Delta\lambda \approx 1500$–$2000$) of the $^{12}CO_2$ molecule in the solid state as observed by the Short-Wavelength Spectrometer (SWS) instrument on board *ISO*. An extensive analysis of the features of $^{13}CO_2$ is presented by Boogert et al. (1999). Section 2 contains a description of the methods used to derive the spectra. In § 3, the observed features are presented and are analyzed through the use of laboratory spectra, and the derived CO_2 abundances are compared with those of other known components of icy grain mantles. Finally, the implications for grain mantle chemistry in the ISM are discussed in § 4.

2. DATA REDUCTION

ISO was launched on 1995 November 17, and the SWS has obtained the first interstellar spectra to span the entire mid-IR wavelength regime ($\lambda = 2.38$–45.2 μm). The SWS instrument consists of two grating spectrometers that use a 100 line mm^{-1} grating in the first 4 orders from 2.4 to 13 μm, and a 30 line mm^{-1} grating in the first 2 orders from 11 to 45 μm (de Graauw et al. 1996a).

Two SWS Astronomical Observing Templates (AOTs) were used to obtain data in the spectral regions containing the fundamental CO_2 absorptions ($\lambda = 4$–4.5 μm, and 12–16 μm). AOT SWS01 observes the full wavelength range from 2.38 to 45.2 μm with one of four different speeds that determine the resulting spectral resolution and sensitivity. Scan times are approximately $\frac{1}{4}$, $\frac{1}{2}$, 1, and 2 hr with respective resolving powers of $\frac{1}{8}$, $\frac{1}{8}$, $\frac{1}{4}$, and $\frac{1}{2}$ of the full SWS resolution (which ranges from 1000 to 2000, depending on the wavelength region; see de Graauw et al. 1996a). AOT SWS06 is designed for smaller wavelength regions with longer integration times at full resolution. Integration times in SWS06 depend on the required sensitivity. A detailed description of the SWS instrument, its calibration, and data reduction techniques can be found in de Graauw et al. (1996a), Schaeidt et al. (1996), and Valentijn et al. (1996).

Details of our observations are listed in Table 1. Data presented in Figures 1, 2, 3, and 4 were obtained in AOTs SWS01 and SWS06 in instrument bands 2A ($\lambda = 4.08$–5.3 μm) and 3A ($\lambda = 12.0$–16.5 μm). The SWS observing modes and integration times for each observation are listed in Table 1. The full spectral resolution in SWS bands 2A and 3A are $\lambda/\Delta\lambda \approx 1800$ and 2000, and therefore our observations carried out with AOT SWS01 speeds 3 and 4 correspond to $\lambda/\Delta\lambda \sim 500$ and 1000, respectively. Wavelength scanning in an observation is achieved by the rotation of a flat mirror located near each grating. Every region of the spectrum is scanned at least twice, in pairs of "up" and "down" scans whose names refer to the scan direction in wavelength space.

The data reduction techniques developed at SRON in Groningen, the SIDT at VILSPA, Spain, and MPE in Garching, Germany, were used to derive the optical depth spectra. Dark currents for each detector over the total scan time were removed by the interpolation of measurements taken at the beginning and end of each scan. Data were converted to astronomical flux density units (Jy) from instrument signal level (μV) by division of the relative spec-

TABLE 1

OBSERVING PARAMETERS

SOURCE	POSITION (J2000) R.A.	POSITION (J2000) decl.	DATE	REVOLUTION[a]	AOT[b]	Δt_{int} [s][c] 4.27 μm	Δt_{int} [s][c] 15.2 μm
W3 IRS 5	02 25 40.8	62 05 52	1997 Jan 17	427	1.3	117	333
			1997 Jan 17	427	6	250	417
GL 490	03 27 38.7	58 47 01	1997 Aug 17	640	1.3	117	192
			1998 Mar 27	863	6	292	384
Elias 16	04 39 38.9	26 11 27	1997 Oct 1	686	6	3883	725
GL 4176	13 43 02.1	−62 08 52	1996 Mar 13	117	6	240	275
			1996 Sep 18	306	6	304	389
Elias 29	16 27 09.3	−24 37 21	1996 Aug 9	267	1.3	117	192
			1996 Sep 3	292	6	496	...
Sgr A*	17 45 40.0	−29 00 28	1996 Feb 19	94	1.4	250	404
GCS 3 I	17 46 14.9	−28 49 34	1996 Oct 8	327	6	507	...
GCS 4	17 46 15.6	−28 49 47	1996 Sep 9	297	1.3	117	192
W33 A	18 14 39.4	−17 52 01	1996 Oct 10	329	1.4	235	384
			1997 Feb 25	467	6	981	389
GL 2136	18 22 26.3	−13 30 08	1996 Mar 16	120	6	477	344
			1996 Sep 23	311	6	240	...
GL 2591	20 29 24.7	40 11 19	1995 Dec 15	28[d]	6	833	417
			1996 Nov 7	357	1.3	117	192
S140	22 19 18.1	63 18 47	1996 Jun 24	220	1.4	234	384
			1996 Aug 6	263	6	501	341
NGC 7538 IRS 1	23 13 45.3	61 28 10	1996 Aug 25	283	6	283	368
			1996 Dec 6	385	1.3	117	192
NGC 7538 IRS 9	23 14 01.6	61 27 20	1996 Feb 23	98	6	2003	384

NOTE.—Units of right ascension are hours, minutes, and seconds, and units of declination are degrees, arcminutes, and arcseconds.

[a] *ISO* revolution (orbit) number during which the data were taken.

[b] "AOT 1.x" indicates an AOT SWS01 observation at speed x.

[c] Time dedicated to the regions containing the IR features of CO_2 (λ = 4.1–4.4, 14.0–16.5 μm).

[d] Data taken in the preverification phase of the *ISO* mission.

tral response function (RSRF) for each SWS band. The wavelength dependence of the RSRF is highly oscillatory in SWS bands 3A through 3D (12–30 μm; see de Graauw et al. 1996a), and if the observed data are shifted in wavelength with respect to the calibration data, a beating or "fringing" pattern results when the RSRF is divided out. Fringing effects were minimized using an interactive routine that applied small wavelength shifts to the response curves before the division. In most cases, however, some small amount of fringing did remain in the spectra. If reliable analyses were still possible, this residual fringing was not removed since attempts to do so (such as clipping high-frequency components from the Fourier transform) slightly alter the shape of existing absorptions. However, the 15.2 μm spectra of NGC 7538 IRS 1, GL 4176, and GL 2591 did require this procedure to remove enough of the fringing to properly analyze them. One artifact appears in all spectra at 14.5 μm (a quasi absorption feature with an optical depth of about 0.05; it is prominent in the spectra of GCS 4, GL 2591, GL 490, and Sgr A*; see Figs. 1, 2, 3, and 4). Its central wavelength corresponds to a discontinuity present in the RSRF, and therefore its removal is quite difficult (see Fig. 1).

Scans in each SWS band free of obvious glitch effects or anomalous response jumps were combined and fit with a straight line. This line was then used to flat-field each scan individually. Up and down scans were independently flat-fielded to correct for anomalous trends in dark current, and final spectra were obtained by an average (weighted by variance) of each up/down pair.

2.1. *Continuum Determination*

Continuum fits in the 4 μm region were obtained by fitting a low-order polynomial (1–3) to data points from 4.0 to 4.1 and 4.4 to 4.5 μm. Since the bending mode at 15.2 μm is located on the short-wavelength edge of the 18 μm silicate absorption, a fit was first made to the continuum from 14 to 25 μm using a low-order polynomial with points from 14 to 14.5 and about 18 to 25 μm (depending on the position and extent of the silicate feature). The silicate feature was subtracted by fitting its shape with a Gaussian curve. As an example, continuum fits to the AOT SWS01 data of S140 are shown in Figure 5.

Toward Elias 29, GL 490, GL 2136, NGC 7538 IRS 1, Sgr A*, S140, W3 IRS 5, and W33 A, another feature of unknown origin centered near 16.4 μm became apparent after the subtraction. This absorption was also fit with a Gaussian curve and subtracted out to produce the final optical depth spectra. It is likely that this feature is merely the result of the jump from SWS band 3A to 3C.

The 15.2 μm features in laboratory spectra typically contain a long-wavelength wing extending to about 16.3 μm. It is not clear whether this occurs in the SWS spectra: it may be hidden by the silicate bending mode in this region. Making a proper continuum fit is therefore not straightforward. In order to estimate error bars on the areas of the 15.2 μm features, we have also made local continuum fits to data points in the ranges 13–14 μm and 16.5–18 μm using low-order polynomials. Such a fit is also shown in Figure 5. The areas of the resulting 15.2 μm bending modes in Figure 5

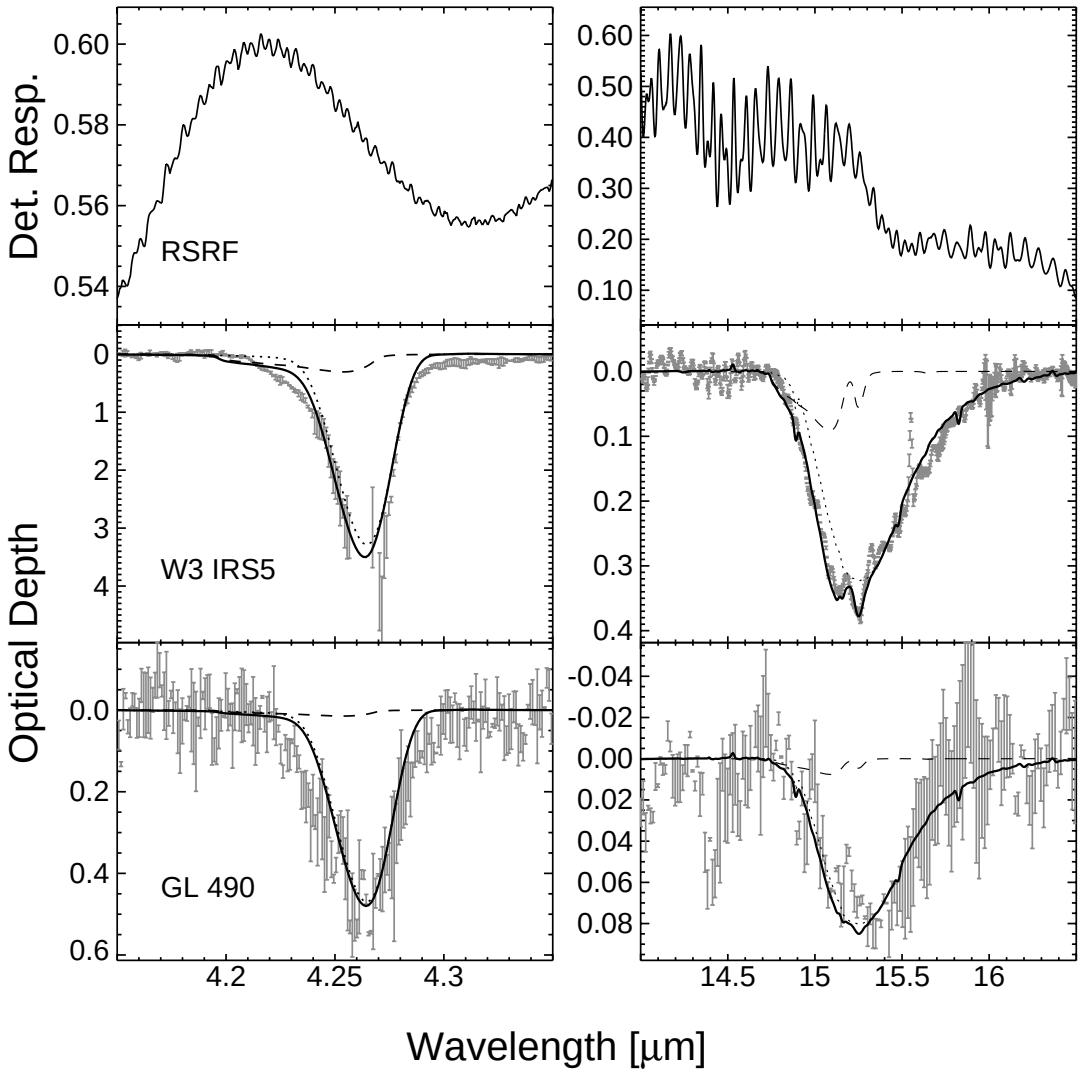

FIG. 1.—*Top panels:* Relative spectral response function (RSRF) for *ISO* SWS detectors in the observed spectral regions. Other panels contain (*left panels*) the observed stretching modes and (*right panels*) bending modes of solid CO_2 toward (*middle panels*) W3 IRS 5 and (*bottom panels*) GL 490 and the best polar + nonpolar lab fits to all features in each case—including the 4.38 μm $^{13}CO_2$ stretching feature (not shown; see Boogert et al. 1999). Dotted lines show polar components of lab fits; dashed lines show nonpolar components; solid lines show sum of polar and nonpolar components. The CO_2 stretching mode of W3 IRS 5 is saturated (flux at the peak wavelength is too low to be measured) and points with signal-to-noise ratios (S/N) < 1 have been omitted. The 15 μm spectrum of W3 IRS 5 contains an emission feature at 15.55 μm due to the fine-structure line of [Ne III]. Apparent absorptions near 14.5 μm are due to imperfect ratioing of a highly fringed feature present in the RSRF (see *top right panel*).

are different by 17%. Error bars in column density (§ 3.4) reflect this uncertainty in continuum shape in lines of sight where the 4.27 μm stretching mode is saturated.

Finally, the source of radiation in the line of sight toward Elias 16 is a background K 1 III star, and its spectrum contains photospheric absorption features at 4.295, 4.352, and 4.393 μm (Whittet et al. 1998). Cancellation of these lines was carried out by ratioing the flux spectrum of Elias 16 by that of HR 8657, a K 2 III star with low extinction.

3. ANALYSIS OF OBSERVED ABSORPTION FEATURES

Observed spectra for all sources are shown in Figures 1, 2, 3, and 4 with the polar:nonpolar fits (§ 3.3.1) and in Figures 6, 7, 8, and 9 with the polar:annealed fits (§ 3.3.2). Tables 2 and 3 list their characteristics. In some cases, the bending mode was unobservable because of low flux levels (e.g., Elias 16) or was too weak to distinguish from fringing or noise in the spectrum (e.g., GCS 4 and GL 4176). An extensive study of the corresponding interstellar $^{13}CO_2$ spectra may be found in Boogert et al. (1999), who present a separate, complementary analysis to that which follows in §§ 3.1–3.5.

3.1. *Observational Characteristics*

The 4.27 μm feature is clearly saturated toward NGC 7538 IRS 9, W3 IRS 5, and W33 A (see Figs. 1, 2, 3, and 4). Sources Elias 29, GL 2136, GL 2591, and GL 4176 exhibit a shallow shoulder ($\tau \approx 0.1$) on the long-wavelength side of the feature, and it is suspected that this is the result of an unidentified, broad underlying component. On the short-wavelength side of the feature, most sources display a wing likely due to a large nonpolar component as seen in laboratory ices containing pure CO_2 (Sandford & Allamandola 1990; Ehrenfreund et al. 1997). The spectra of GL 2136, GL 2591 and GL 4176 also contain shallow absorption shoulders on the short- and long-wavelength sides of the stretch-

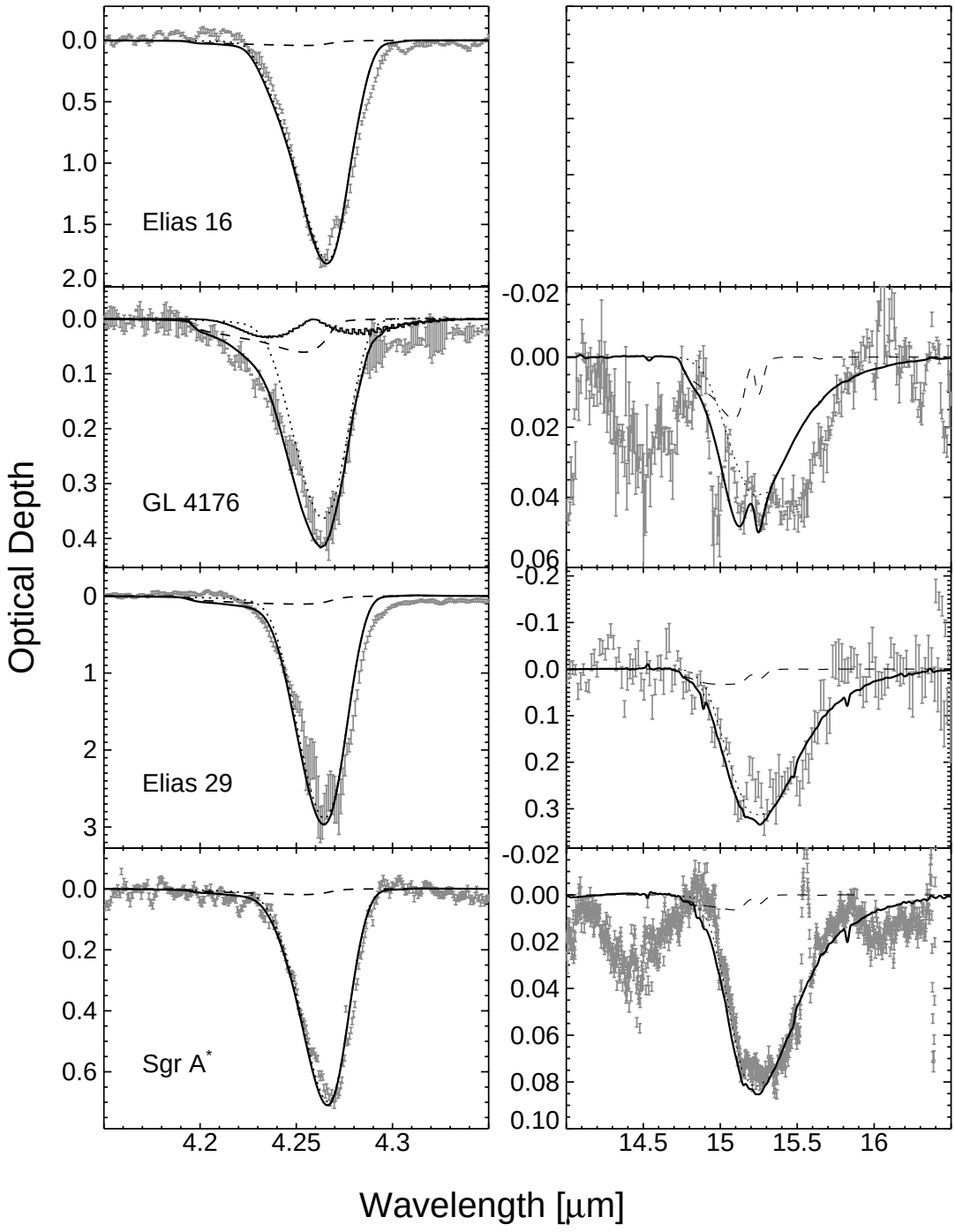

FIG. 2.—Interstellar solid CO_2 spectra and best polar + nonpolar lab fits presented as in Fig. 1, but for Elias 16, GL 4176, Elias 29, and Sgr A*. Gas-phase CO_2 absorption at 4.27 μm has been estimated for GL 4176 using the 14.97 μm CO_2 gas feature. Spurious structure exists in the troughs of the Elias 16 and Elias 29 stretching modes because of low flux levels. Observations of Elias 16 near 15 μm were precluded by its low continuum flux. The 15 μm spectrum of Sgr A* contains an emission feature at 15.55 μm due to the fine-structure line of [Ne III].

ing mode. These absorptions are likely due to the unresolved *P*- and *R*-branches of gas-phase CO_2, consistent with the strong gas-phase ν_2 absorptions seen at 14.97 μm toward these sources. Estimated underlying gas components are plotted in Figures 1, 2, 3, and 4 and have been subtracted from the spectra before performing the laboratory fits (§ 3.3). The apparent "emission" in the spectrum of Elias 16 at 4.22 and 4.27 μm is not real but the result of differences in the up and down scans of this observation (because of the low flux level of this object at these wavelengths). Spurious structure also exists in the troughs of the 4.27 μm features of Elias 29 and NGC 7538 IRS 1, which may be close to saturation.

The observed CO_2 15.2 μm bending modes (Figs. 1, 2, 3, and 4) have at least two peaks toward most sources: apart from those with poor signal-to-noise ratio, the only exception is Sgr A*. Toward GL 2136, GL 2591, GL 4176, NGC 7538 IRS 1, NGC 7538 IRS 9, Sgr A*, W3 IRS 5, and W33 A, absorption due to the *Q* branch of the gas-phase CO_2 ν_2 band can be seen at 14.97 μm with a width of about 0.02 μm.

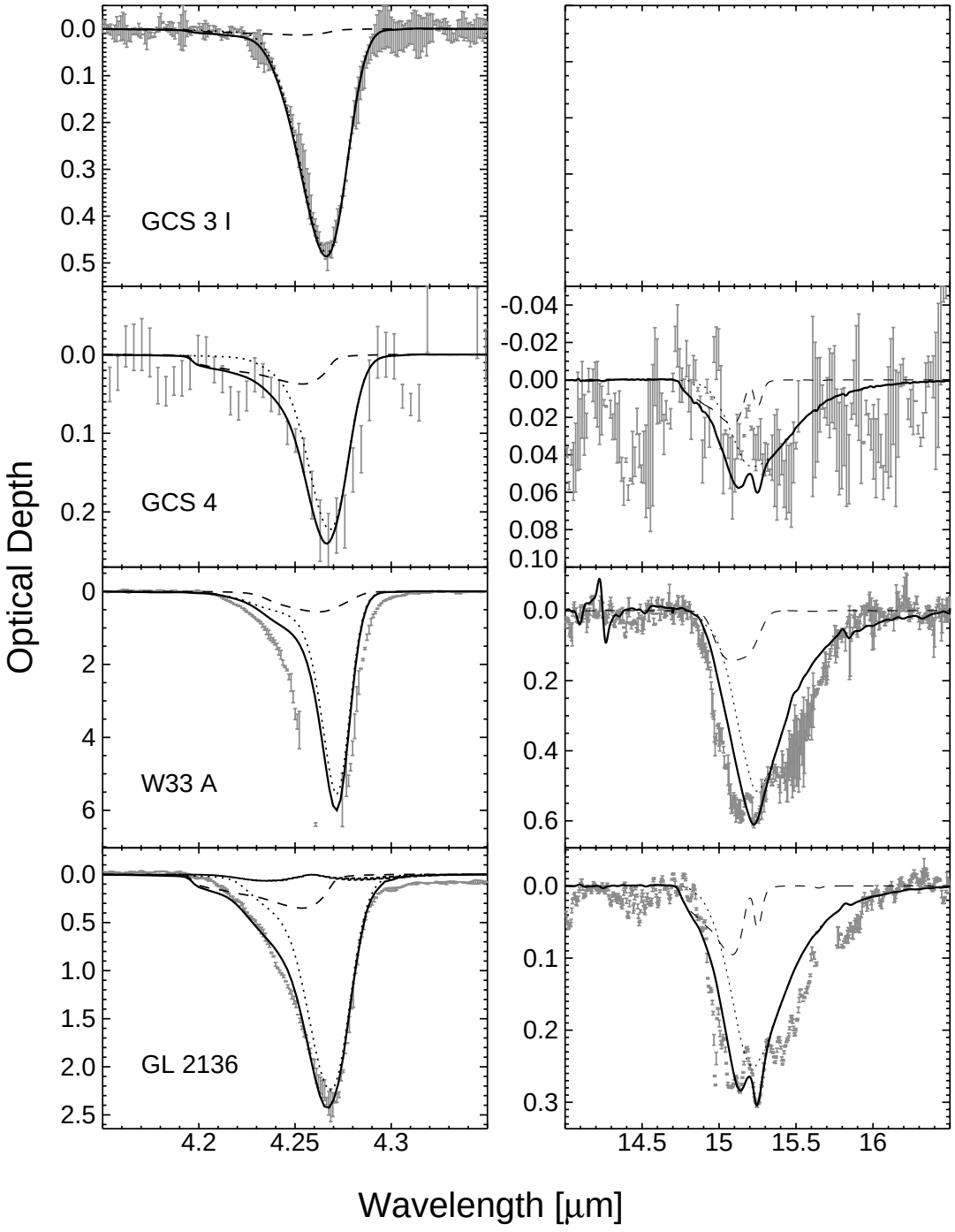

FIG. 3.—Interstellar CO_2 spectra and best polar + nonpolar lab fits presented as in Fig. 1, but for GCS 3 I, GCS 4, W33 A, and GL 2136. No 15 μm data exist for GCS 3 I. The spectrum of GCS 4 contains emission at 15.55 μm (beyond the flux scale of the plot) due to the fine-structure line of [Ne III]. The stretching mode of W33 A is saturated (peak flux is too low to be measured), and points with S/N < 1 have been omitted. Gas-phase CO_2 absorptions at 4.27 μm have been estimated for GL 2136 using the 14.97 μm CO_2 gas feature.

The gas-phase CO_2 features toward GL 2591 and GL 4176 may have been broadened by attempts to remove fringing (§ 2), but their widths could also be due to high CO_2 excitation temperatures toward these sources. The gas-phase CO_2 data will be further analyzed and discussed by Boonman et al. (1999). At this resolution, all Q-branch ro-vibrational lines merge into one apparent absorption feature. This unresolved band is easier to observe than the corresponding gas-phase ν_3 band at 4.27 μm, which is intrinsically 10 times stronger but has only P- and R-branch structure (van Dishoeck et al. 1996). The spectra of W3 IRS 5, Sgr A*, and GCS 4 also contain the fine-structure line of doubly ionized neon [Ne III] at 15.55 μm, indicating the presence of ionized gas (an H II region) in these lines of sight.

In general, the profiles of all the observed interstellar 15.2 μm features can be broken down into three components: a broad underlying feature (observed $\Delta\nu = 16.3$–27.4 cm^{-1} vs. ≈ 25 cm^{-1} in the lab), a pair of sharp peaks at 15.15 and

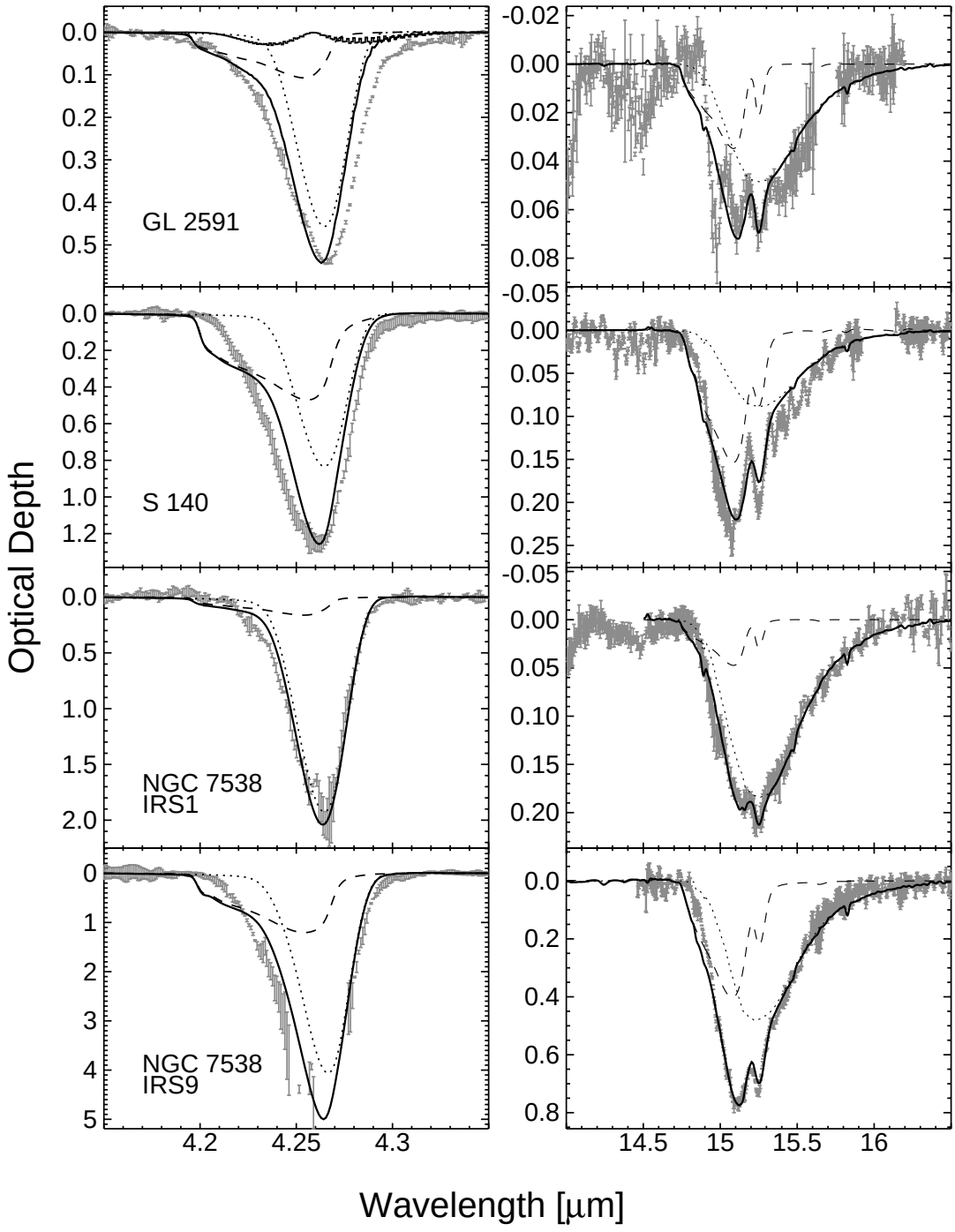

FIG. 4.—Interstellar CO_2 spectra and best polar + nonpolar lab fits presented as in Fig. 1, but for GL 2591, S140, NGC 7538 IRS 1, and NGC 7538 IRS 9. Gas-phase CO_2 absorptions at 4.27 μm have been estimated for GL 2591 using the 14.97 μm CO_2 gas feature. Structure in the trough of the NGC 7538 IRS 1 stretching mode is due to low flux levels. The stretching mode of NGC 7538 IRS 9 is saturated (peak flux is too low to be measured), and points with S/N < 1 have been omitted.

15.27 μm (observed $\Delta\nu = 1.7$–6.6 cm^{-1} vs. $\approx$2–4 cm^{-1} in the lab), and a shoulder near 15.4 μm (laboratory measurements from Ehrenfreund et al. 1997). The relative contributions of these components vary from source to source. For example, the height of the peaks near 15.15 and 15.27 μm are highly variable and measure up to 40% of the total peak optical depth (in S140). Toward GL 2136, GL 4176, NGC 7538 IRS 1, S140, W3 IRS 5, and W33 A (and weakly toward NGC 7538 IRS 9), a third peak or broad shoulder is apparent on the long-wavelength side of the 15.2 μm feature at approximately 15.4 μm. In most cases this absorption is broad and shallow, but it appears sharply peaked toward GL 2136.

We attribute the broad underlying component to CO_2 in a polar environment (presumably an H_2O- and/or CH_3OH-rich ice). The two sharp peaks at 15.15 and 15.27 μm have been shown to form in annealed CO_2 ices and in certain nonpolar ice mixtures upon warm-up (Sandford & Allamandola 1990; Ehrenfreund et al. 1997). In the latter, ice segregation is taking place; this forms a CO_2 ice that is

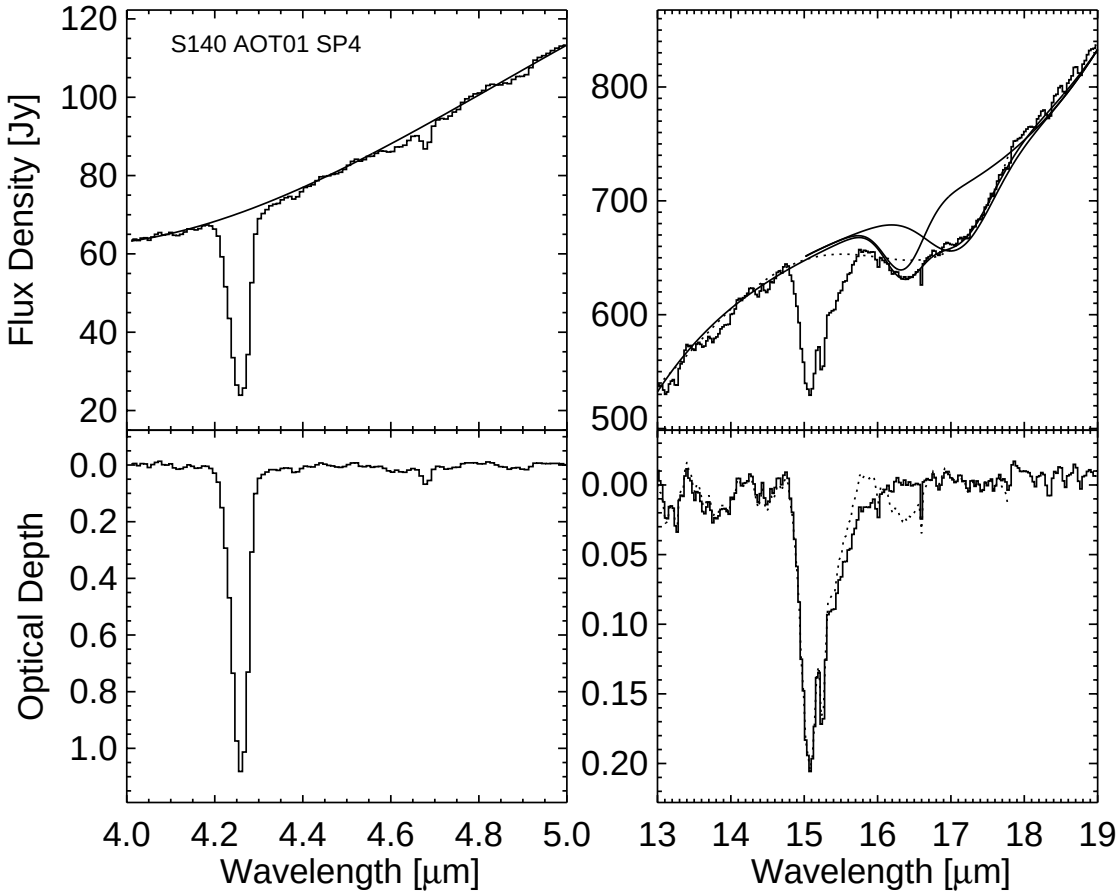

FIG. 5.—Demonstration of continuum fits using the AOT SWS01 speed 4 data of S140. *Left panels:* CO_2 stretching mode region. *Right panels:* CO_2 bending mode region. In the 15.2 μm region, two extreme cases are given by the solid and dotted lines. The solid lines represent a third-order polynomial fit to continuum between 13–14 and 18–19 μm combined with Gaussian fits to the structure of the 16–18 μm feature. The dotted line is a fifth-order polynomial fit to points adjacent to the CO_2 feature.

embedded in the matrix of the other component. The broad shoulder does not seem to correlate with the other components, and recent lab results (Ehrenfreund et al. 1999) indicate that this absorption may be a result of CO_2:CH_3OH ice complexes (cf. § 3.3).

3.2. *Laboratory Data*

Laboratory experiments by Sandford & Allamandola (1990) and Ehrenfreund et al. (1997) have shown that at 10 K the bending mode consists of one broad absorption for

TABLE 2

PROPERTIES OF OBSERVED 4.27 μm FEATURES

SOURCE	ν_0 (μm)	ν_0 (cm^{-1})	τ_0	$\Delta\nu$ (cm^{-1})	S/N[a]	COMMENTS[b]
W3 IRS 5	...	...	>3	~20	28	Saturated
GL 490	4.262	2346.2	0.46 ± 0.05	21.3	27	
Elias 16	4.265	2344.6	$1.8^{+0.5}_{-0.2}$	19.6	63	Long-λ wing
GL 4176	4.264	2345.4	0.40 ± 0.02	17.8	97	Long-λ wing
Elias 29	4.267	2343.5	2.77 ± 0.2	17.1	49	
Sgr A*	4.269	2342.3	0.70 ± 0.01	16.7	100	Short-λ wing, 4.38 μm H em
GCS 3 I	4.267	2343.3	0.48 ± 0.02	15.4	67	
GCS 4	4.270	2342.0	0.22 ± 0.02	12.8	40	
W33 A	...	...	>5	~20	58	Saturated
GL 2136	4.269	2342.7	2.40 ± 0.08	18.5	144	
GL 2591	4.266	2344.3	0.55 ± 0.01	24.0	215	Broad, short- & long-λ wings
S140	4.262	2346.5	1.25 ± 0.04	23.9	50	
NGC 7538 IRS 1	4.265	2344.7	2.03 ± 0.11	16.4	40	
NGC 7538 IRS 9	...	...	>5	~20	15	Saturated

[a] Median signal-to-noise ratio across the range of the feature.

[b] "Saturated" indicates an optical depth too great to be measured by *ISO* SWS.

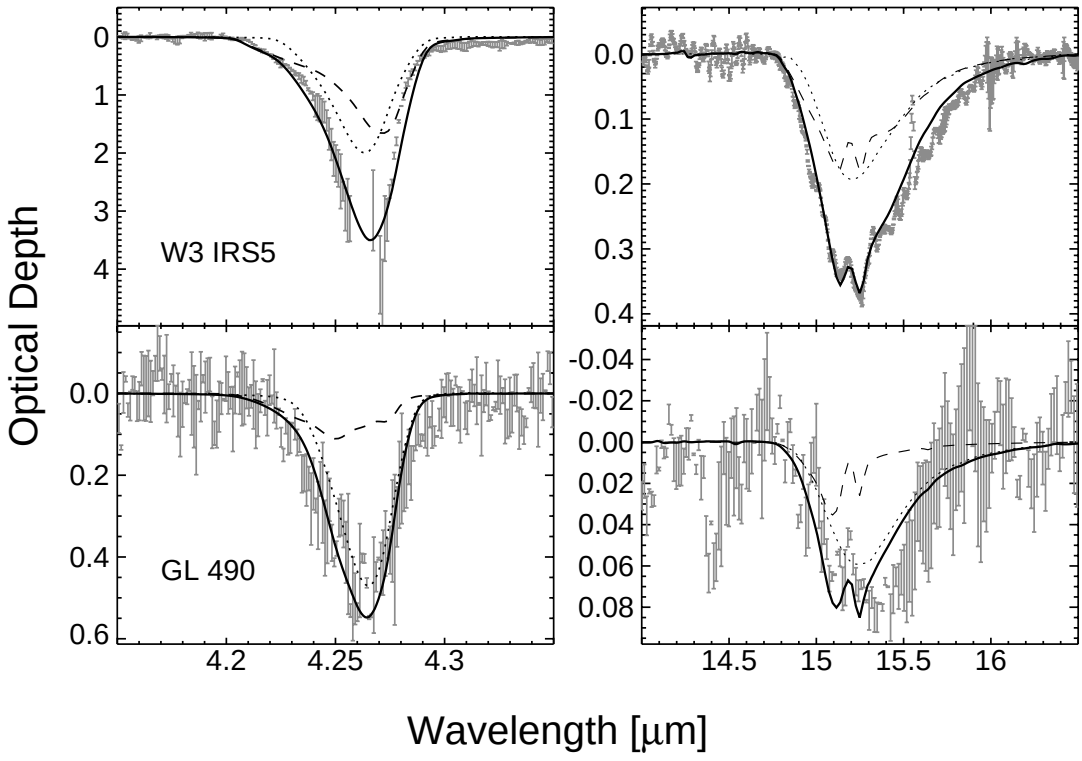

FIG. 6.—Interstellar solid CO_2 spectra toward W3 IRS 5 and GL 490, and the best lab fits with polar + annealed methanol-rich ices to all features—including the 4.38 μm $^{13}CO_2$ stretching feature (not shown)—in each case. Dotted lines show polar components; dashed lines show annealed components; solid lines show sum of polar and annealed components.

TABLE 3

PROPERTIES OF OBSERVED 15.2 μm FEATURES

SOURCE	ν_i[a] (μm)	ν_i[a] (cm^{-1})	τ_i	$\Delta\nu_i$[b] (cm^{-1})	$\Delta\nu$[c] (cm^{-1})	S/N[d]	COMMENTS[e]
W3 IRS 5	15.26	655.3	0.37 ± 0.01	3.2	24.6	260	Weak gas, weak shoulder
	15.14	660.7	0.34 ± 0.01	2.5			[Ne III] emission
GL 490	15.34	651.7	0.08 ± 0.02	...	22.2	87	Broad, single peak
GL 4176.....	15.27	654.8	0.047 ± 0.003	2.5	26.3	500	Strong gas, strong shoulder
	15.14	660.7	0.044 ± 0.003	3.0			FFT
Elias 29.....	15.29	654.2	0.33 ± 0.02	1.9	23.1	42	Strong shoulder
	15.12	661.4	0.30 ± 0.01	4.0			
Sgr A*.....	15.28	654.5	0.077 ± 0.005	2.1:	20.3	500	Broad single peak, [Ne III] emission
	15.1:	662:	0.08:	1.7:			Possible 2nd peak
GCS 4	15.3:	652:	0.04 ± 0.01	...	19:	90	Very strong [Ne III] emission
	15.1:	662:	0.05 ± 0.01	...			
W33 A.....	15.24	656.3	0.58 ± 0.01	2.8	27.4	108	Mod. gas, strong shoulder
	15.14	660.7	0.57 ± 0.02	4.3			
GL 2136.....	15.24	656.0	0.30 ± 0.01	2.9	24.5	500	Strong gas, strong shoulder
	15.11	662.0	0.28 ± 0.01	4.9			
GL 2591.....	15.24	656.0	0.073 ± 0.005	2.8	25.1	307	Very strong gas
	15.11	661.8	0.068 ± 0.005	3.2			Strong shoulder, FFT
S140	15.25	655.8	0.21 ± 0.01	3.1	16.3	136	Narrow, sharp peaks
	15.09	662.9	0.24 ± 0.02	6.6			
NGC 7538 IRS 1.....	15.24	656.1	0.21 ± 0.01	3.5	24.3	139	Weak gas, weak shoulder
	15.14	660.5	0.19 ± 0.01	1.8			Weak [Ne III] emission, FFT
NGC 7538 IRS 9.....	15.25	655.9	0.736 ± 0.005	2.2	21.1	101	Weak gas
	15.10	662.1	0.766 ± 0.005	4.3			

[a] Values marked with colons have high degrees of uncertainty.

[b] FWHM relative to the underlying broad component.

[c] Width of the entire feature.

[d] Median signal-to-noise ratio across the range of the feature.

[e] "FFT" indicates that fringing has been removed by clipping frequencies from the Fourier transform of the data (see § 2). "[Ne III] emission" indicates the presence of Ne fine-structure emission at 15.55 μm.

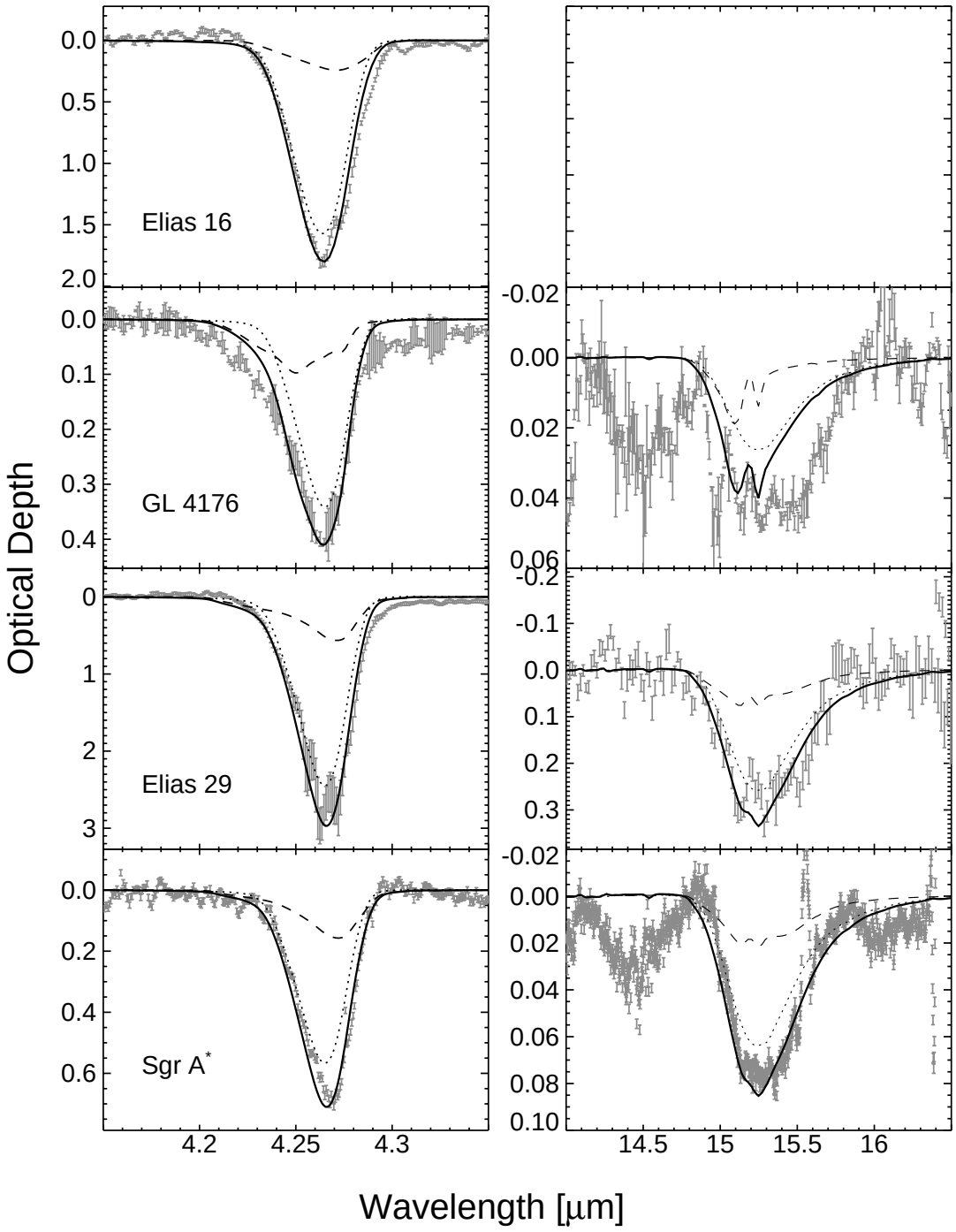

FIG. 7.—Polar + annealed laboratory fits to the CO_2 spectra toward Elias 16, GL 4176, Elias 29, and Sgr A*. Lines are as in Fig. 6.

all ice mixtures studied, with the exception of pure CO_2, which is doubly peaked. This vibration is doubly degenerate and splits when the axial symmetry of the molecule is broken. CO_2 is known to form T-shaped complexes with a variety of molecules, leading to very broad bands (e.g., CO_2:CH_3OH complexes). Upon warm up of such mixtures, multipeaked structures form in all CO_2 absorption features (Ehrenfreund et al. 1999). The exact positions and widths of these peaks vary according to ice matrix and thereby greatly constrain the composition of the ice mixture (see § 3.3).

The $^{13}CO_2$ asymmetric stretching mode is, like the 15.2 μm bending mode, an extremely sensitive diagnostic of the ice matrix (Ehrenfreund et al. 1997; Boogert et al. 1999). While it is the splitting of the 15.2 μm band that indicates ice composition, both the peak position and width of the $^{13}CO_2$ stretching mode are strongly dependent on ice composition; polar and nonpolar components may be easily distinguished.

3.3. *Laboratory Fits to Observational Data*

All spectra were matched to a suite of laboratory data from the Leiden Observatory Laboratory (Ehrenfreund et al. 1996, 1997, 1999), applying a χ^2_ν minimization method similar to that used by Chiar et al. (1994, 1995) to fit solid-state CO features toward the Serpens and Taurus dark

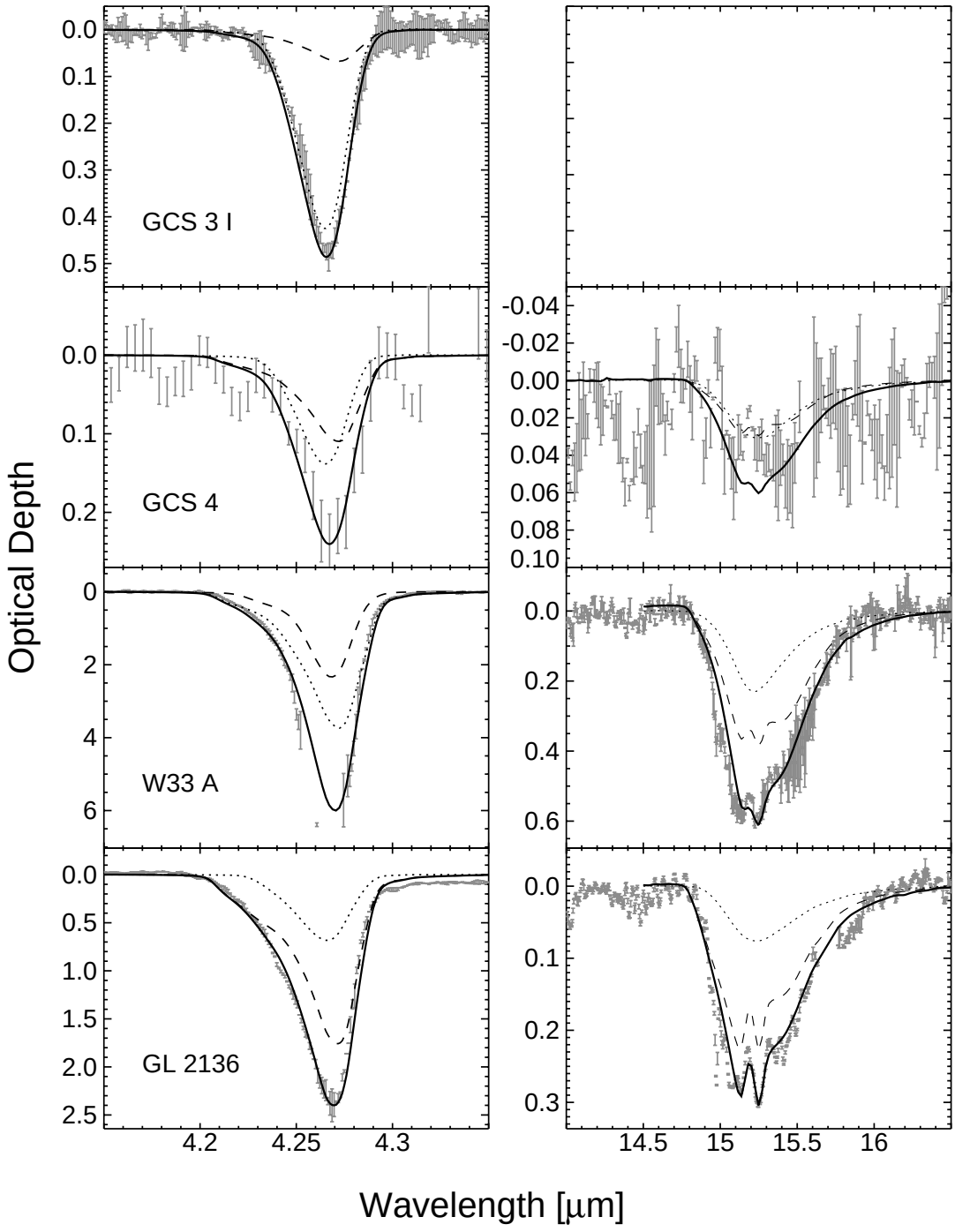

FIG. 8.—Polar + annealed laboratory fits to GCS 3 I, GCS 4, W33 A, and GL 2136. Lines are as in Fig. 6.

clouds. Particle shape corrections were applied to the lab data using four different grain models derived from the real and imaginary parts of the ice's refractive index (for a detailed discussion of the calculation procedure, see Ehrenfreund et al. 1997). In general, we find that a continuous distribution of ellipsoids, where each shape is equally probable, gives the best fit.

Laboratory mixtures considered in the fits are separated into three categories: polar, nonpolar, and annealed ices; see Table 4 for a complete listing. Polar ices are dominated by H_2O, and include mixtures such as $H_2O:CO_2 \approx 100:15$ and 1:1, $H_2O:CH_3OH:CO_2 \approx 100:40:60$ and 100:10:15 (at various temperatures from 10 to 80 K). Nonpolar ice mixtures come from Ehrenfreund et al. (1997) and include a wide variety of ice compositions dominated by the molecules CO_2, CO, O_2 and N_2. Nonpolar ice temperatures are 10 and 30 K except where the mixture is dominated by CO_2, in which case temperatures of 50 and 80 K are also included. Certain nonpolar mixtures contain a trace amount of H_2O (1%–10%). The annealed ices have the approximate composition of $H_2O:CH_3OH:CO_2 = 1:1:1$ upon initial deposition at 10 K and have been heated to high temperatures (80–145 K). These spectra show a complicated structure in all CO_2 features due to crystallization and annealing of the various ice components and therefore cannot be discretely classified as either polar or nonpolar.

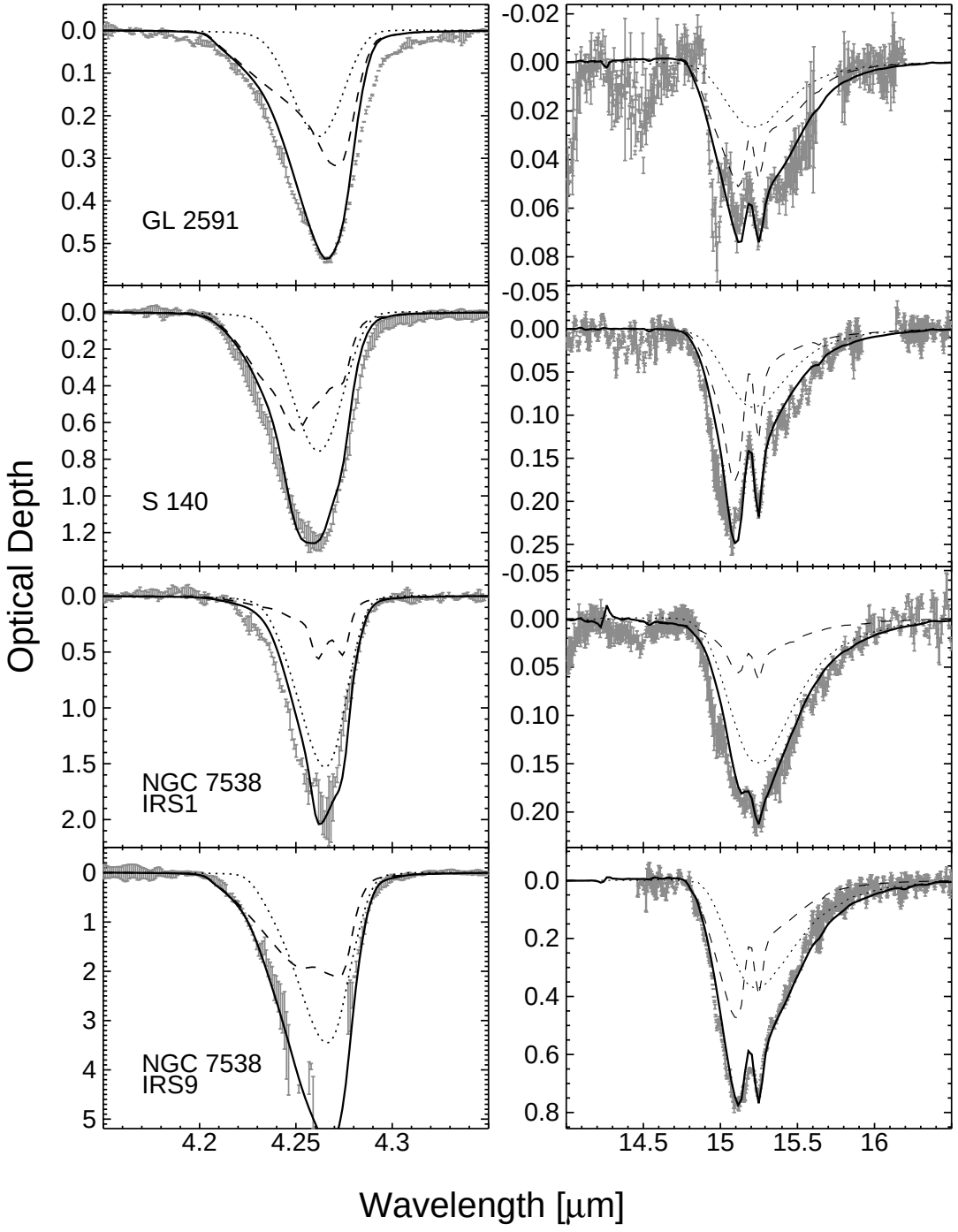

FIG. 9.—Polar + annealed laboratory fits to GL 2591, S140, NGC 7538 IRS 1 and NGC 7538 IRS 9. Lines are as in Fig. 6.

These data will be analyzed in detail in a laboratory study by Ehrenfreund et al. (1999).

The laboratory fits that give the best agreement to all three absorption features in each source are listed in Table 5 (polar:nonpolar fits) and Table 6 (polar:annealed fits). Corresponding spectra are shown in Figures 1, 2, 3, and 4 and 6, 7, 8, and 9. The results of these fits indicate that two chemically different CO_2 ice components exist along these lines of sight—one dominated by H_2O (polar), and another dominated by CO_2 itself (nonpolar or annealed). We find that the height and sharpness of the 15.2 μm feature's subpeaks and the positions and widths of the 4.38 μm feature's two components are the most sensitive indicators of the CO_2 ice environment and thereby give the most stringent constraints to the resulting fits.

3.3.1. *Polar:Nonpolar fits*

Fits to the observed CO_2 features have been made in order to determine the ice environment(s) in the studied lines of sight. Since it has been shown that solid interstellar CO exists in both polar and nonpolar ice phases (Tielens et al. 1991; Chiar et al. 1995, 1998), we have attempted similar fits to the interstellar CO_2 features observed here. In conducting the polar:nonpolar fits, general agreement could be

TABLE 4

LABORATORY MIXTURES USED IN FITS

Mixture	Laboratory T (K)
Polar (from Ehrenfreund et al. 1997 and Leiden Obs. Lab. Database)	
$H_2O:CO_2 = 100:14$	10, 50, 80
$H_2O:CO_2 = 100:125$	10, 30, 50, 80, 125
$H_2O:CO:CO_2 = 100:3:20$	20
$H_2O:CH_3OH:CO_2 = 100:40:60$	10, 50, 80, 140
$H_2O:CH_3OH:CO_2 = 100:10:15$	10, 50, 80, 120
Annealed (from Ehrenfreund et al. 1999)	
$H_2O:CH_3OH:CO_2 = 1:1:1$	10, 65, 80, 90, 96, 105, 106, 110, 111, 112, 115, 116, 117, 118, 119, 120, 121, 123, 130, 136, 145
Nonpolar (from Ehrenfreund et al. 1997)	
Pure CO_2	10, 50, 80
$H_2O:CO_2 = 1:100$	10, 30
$H_2O:CO_2 = 1:10$	10, 80
$H_2O:CO_2 = 1:6$	10, 50, 75
$CO:CO_2 = 100:4$	10, 30
$CO:CO_2 = 100:8$	10, 30
$CO:CO_2 = 100:16$	10, 30
$CO:CO_2 = 100:21$	10, 30
$CO:CO_2 = 100:23$	10, 30
$CO:CO_2 = 100:26$	10, 30
$CO:CO_2 = 100:70$	10, 30
$H_2O:CO:CO_2 = 1:50:56$	10, 45
$CO_2:O_2 = 1:1$	10
$CO:O_2:CO_2 = 100:50:4$	10, 30
$CO:O_2:CO_2 = 100:50:8$	10
$CO:O_2:CO_2 = 100:50:16$	10, 30
$CO:O_2:CO_2 = 100:50:21$	10, 30
$CO:O_2:CO_2 = 100:50:32$	10
$CO:O_2:CO_2 = 100:54:10$	10, 30
$CO:O_2:CO_2 = 100:20:11$	10, 30
$CO:O_2:CO_2 = 100:11:20$	10, 30
$CO:O_2:CO_2 = 100:10:23$	10, 30
$CO:N_2:CO_2 = 100:50:20$	10, 30
$CO:O_2:N_2:CO_2 = 100:50:25:32$	10, 30
$H_2O:CO:O_2:N_2:CO_2 = 1:50:35:15:3$	10
$H_2O:CO:O_2:N_2:CO_2 = 1:25:25:10:13$	10

found between the 15.2 μm bending mode and the feature of $^{13}CO_2$ at 4.38 μm (i.e., the same mixtures with the same relative abundances gave good fits for each band). In the case of W33 A, however, fits to the 15.2 μm feature indicate a polar:nonpolar ratio of about 2, while the $^{13}CO_2$ feature suggests a much higher ratio of 12. Interestingly, the opposite is found for the features of W3 IRS 5, where $^{13}CO_2$ indicates a smaller polar:nonpolar ratio than $^{12}CO_2$ (1.3 vs. 5.0). In each of these cases, a compromise between the two features was taken (see Table 5 and Figs. 1 and 3).

Toward sources with strong nonpolar components, it was difficult to fit the 4.27 μm feature with the same mixtures as the 4.38 and 15.2 μm features. A reasonable fit is possible, but the nonpolar component is always underestimated, or the structure in the 4.38 and 15.2 μm features is not well reproduced. These problems are thought to come from the derivation of the ices' optical constants (n and k), which has been shown to be somewhat controversial. For example, the peak values of n and k derived for the 4.27 μm feature by different laboratories differ by as much as a factor of 2 (Trotta 1996; Ehrenfreund et al. 1997). Moreover, any optical constant errors are magnified by the particle shape corrections in strong absorptions, since the calculated cross sections are proportional to $1/nk$ (see Ehrenfreund et al. 1997, eq. [5]). Where detected with a high enough signal, we take the 4.38 μm feature of $^{13}CO_2$ to be the most reliable indicator of the CO_2 ice environment in these fits, since it is unaffected by particle shape calculations involving the optical constants of the ice. The next most reliable indicator is the 15.2 μm bending mode of $^{12}CO_2$.

Figure 10 contains a plot of the resulting polar fractions of the total CO_2 column density versus the cold gas component temperature measured in these lines of sight (see Table 7). The trend appears to be that less polar CO_2 exists in lines of sight with warmer gas.

3.3.2. *Annealed* $H_2O:CH_3OH:CO_2$ *Fits*

The CO_2 bending mode typically contains a shoulder at 15.4 μm that is not well represented by simple polar:nonpolar constituents (see § 3.3.1 and Figs. 1, 2, 3, and 4). As a means of tracing its source, the observed interstellar spectra have also been compared with those of ther-

TABLE 5

SUMMARY OF POLAR + NONPOLAR LABORATORY FITS

SOURCE	POLAR COMPONENT		NONPOLAR COMPONENT		% NONPOLAR[a]				
	Component	T (K)	Component	T (K)	4.27 μm	4.38 μm	15.2 μm	All	$\chi_\nu^{2\,b}$
W3 IRS 5	$H_2O:CH_3OH:CO_2 = 100:8:14$	10	Pure CO_2	80	13	29	11	13 ± 4	29
GL 490	$H_2O:CH_3OH:CO_2 = 100:8:14$	10	Pure CO_2	80	14	...[c]	<5[d]	<5	2.4
Elias 16	$H_2O:CO:CO_2 = 100:3:20$	20	...		<4	...[e]	...	<4	21
GL 4176	$H_2O:CO_2 = 100:14$	10	Pure CO_2	80	42	...[c]	22	20 ± 3	30
Elias 29	$H_2O:CH_3OH:CO_2 = 100:8:14$	10	$H_2O:CO_2 = 1:100$	30	0.0	0.0	9	7 ± 2	29
Sgr A*	$H_2O:CH_3OH:CO_2 = 100:8:14$	50	...		<5	...[f]	0.0	<5	21
GCS 3 I	$H_2O:CH_3OH:CO_2 = 100:8:14$	50	...		<5	0.0	...	<5	1.2
GCS 4	$H_2O:CH_3OH:CO_2 = 100:8:14$	80	Pure CO_2	80	<23	...[c]	...[f]	<23	3.0
W33 A	$H_2O:CO_2 = 100:125$	125	$CO:CO_2 = 100:70$	10	41	6	30	15 ± 5	392
GL 2136	$H_2O:CO_2 = 100:14$	80	Pure CO_2	80	23	25	30	20 ± 3	408
GL 2591	$H_2O:CH_3OH:CO_2 = 100:8:14$	10	Pure CO_2	80	26	23	20	27 ± 4	103
S140	$H_2O:CH_3OH:CO_2 = 100:8:14$	10	$H_2O:CO_2 = 1:6$	75	62	40	43	50 ± 5	8.6
NGC 7538 IRS 1	$H_2O:CH_3OH:CO_2 = 100:8:14$	10	Pure CO_2	80	27	0.0	12	12 ± 2	4.5
NGC 7538 IRS 9	$H_2O:CH_3OH:CO_2 = 100:8:14$	50	$H_2O:CO_2 = 1:10$	30	15	33	33	34 ± 5	8.1

[a] Percentage of total solid CO_2 contained within the nonpolar component in fits to individual features (indicated by wavelength); "all" lists the best percentage when the three features are fit simultaneously; error bars and upper limits represent the range of equivalent fits.

[b] Calculated for the simultaneous fit to all three features.

[c] S/N or resolution too low for accurate fits to this feature.

[d] Nonpolar upper limits obtained by adding pure CO_2 at or near the temperature of the polar component.

[e] Interference due to stellar photospheric lines prevents accurate fits to this feature.

[f] Interference due to H emission line prevents accurate fits to this feature.

TABLE 6

SUMMARY OF POLAR + ANNEALED LABORATORY FITS

SOURCE	POLAR COMPONENT		ANNEALED T[a]	% ANNEALED[b]				
	Component	T (K)	(K)	4.27 μm	4.38 μm	15.2 μm	All	χ_ν^{2c}
W3 IRS 5	$H_2O:CO_2 = 100:14$	10	136	25	0	68	46 ± 17	33
GL 490	$H_2O:CO_2 = 100:14$	10	136	<25	…[d]	0	<25	1.9
Elias 16	$H_2O:CO_2 = 100:14$	10	10	<17	<40[e]	…	<17	16
GL 4176	$H_2O:CO_2 = 100:14$	10	136	32	0	28	28 ± 10	47
Elias 29	$H_2O:CO_2 = 100:14$	10	117	12	33	58	22 ± 10	14
Sgr A*	$H_2O:CO_2 = 100:14$	10	115	<38	…[f]	<33	<38	19
GCS 3 I	$H_2O:CO_2 = 100:14$	10	115	<26	0	…	<15	1.8
GCS 4	$H_2O:CO_2 = 100:14$	10	115	<65	…[d]	…[f]	<65	2.5
W33 A	$H_2O:CO_2 = 100:14$	80	112	18	26	100	65 ± 15	62
GL 2136	$H_2O:CO:CO_2 = 100:3:20$	20	117	53	100	100	75 ± 25	138
GL 2591	$H_2O:CO_2 = 100:14$	10	117	76	77	54	44 ± 11	32
S140	$H_2O:CO_2 = 100:14$	10	136	62	39	58	52 ± 10	6.2
NGC 7538 IRS 1	$H_2O:CO_2 = 100:14$	10	145	0	21	39	25 ± 8	11
NGC 7538 IRS 9	$H_2O:CO:CO_2 = 100:3:20$	20	119	45	47	44	45 ± 5	8.1

[a] All annealed components consist of the mixture $H_2O:CH_3OH:CO_2 = 1:1:1$.

[b] Percentage of total solid CO_2 contained in the annealed ice component in fits to individual features (indicated by wavelength); "all" lists the best percentage when the three features are fit simultaneously; error bars and upper limits represent the range of equivalent fits.

[c] Calculated for the simultaneous fit to all three features.

[d] S/N or resolution too low for accurate fits to this feature.

[e] Interference due to stellar photospheric lines prevents accurate fits to this feature.

[f] Interference due to H emission line prevents accurate fits to this feature.

mally annealed methanol-rich laboratory ices (which display such a feature; see Fig. 11). These ices are highly inhomogeneous as a result of segregation of the CH_3OH and CO_2 components and are no longer well represented by thin films. Particle shape corrections are therefore not required, and their spectra in the laboratory may be directly compared with interstellar spectra. The physical structure of these ices is described in detail by Ehrenfreund et al. (1999).

In Figure 11, $H_2O:CH_3OH:CO_2 = 1:1:1$ mixtures have been fitted to the observed bending mode spectra. The temperature evolution for this ice shows a remarkable similarity to the *ISO* spectra. At low temperatures, the 15.2 μm feature is broad, with no sharp peaks (Sgr A*). As it is heated, the peaks indicative of pure CO_2 ice appear (NGC 7538 IRS 9) and grow stronger with increasing temperature, showing that the CO_2 molecules are annealing within the polar ice (NGC 7538 IRS 1, W3 IRS 5). When these peaks are strong, the shoulder at 15.4 μm becomes distinct (W33 A, GL 2136). Finally, the nonpolar ices dominate the spectrum at high temperatures, where nearly all of the CO_2 has annealed (S140).

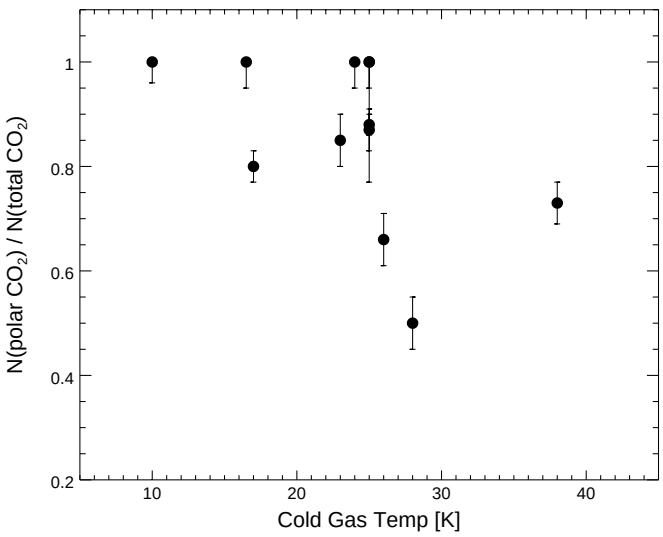

FIG. 10.—Fractions of polar solid CO_2 as derived from the polar + nonpolar laboratory fits (§ 3.3.1) to all CO_2 features vs. line-of-sight cold gas temperatures from Table 7.

While the observed CO_2 spectrum toward each source is well matched by a single $H_2O:CH_3OH:CO_2 = 1:1:1$ ice in this way (Fig. 11), the relative abundances of CH_3OH and CO_2 required do not agree with observations (interstellar $N_{CH_3OH}/N_{CO_2} \lesssim 50\%$; Allamandola et al. 1992; Brooke, Sellgren, & Smith 1996a). Other polar molecules in the ice could invoke this kind of interaction with CO_2, however (Ehrenfreund et al. 1999), and possibly only a fraction of the CO_2 molecules in a given line of sight is needed to produce the observed 15.4 μm shoulders.

Indeed, the CO_2 profiles may also be reproduced by a sum of methanol-rich and methanol-poor ices. The methanol-poor ices provide the broad underlying component, and the annealed methanol-rich ices provide both the sharp double peaks and the 15.4 μm shoulder. In order to constrain the amount of CH_3OH ice required, we have performed two-component fits to the interstellar spectra using the methanol-free polar ices plus the thermally annealed methanol-rich ice listed in Table 4. The fitting procedure is the same as described above for the polar:nonpolar ices (§ 3.3.1). The results are summarized in Table 6 and presented in Figures 6, 7, 8, and 9. In general, fits that matched the bending mode also made good fits to the 4.27 and 4.38 μm features. The amount of annealed CO_2 that gives a good fit to all features in each case is not unique but falls in the range given by the error bars listed in Table 6. Where known, abundances of interstellar CH_3OH (Table 7) are consistent with these values, with the exception of W3 IRS 5, which seems to require a higher abundance of

TABLE 7

COLUMN DENSITIES[a]

SOURCE	CO_2 Total	CO_2 Pol/Npol[b]	CO_2 Pol/Annl[b]	H_2O	CO Total	CO Pol/Npol	CH_3OH	N_H[c] (10^{23} cm^{-2})	Gas T (K)	REFERENCES
W3 IRS 5	7.1 ± 1.8	6.2/0.9	3.8/3.3	54	1.6	<0.5/1.1	<0.8	2.7	25, 577	1, 2, 3, 4
GL 490	1.7 ± 0.3	1.7/<0.1	1.3/<0.4	7.3	1.0	<0.3/0.7	...	0.98	24, 107	1, 2, 5
Elias 16	$4.6^{+1.3}_{-0.6}$[d]	4.6/<0.2	3.8/<0.8	25	6.5	0.8/5.6	<0.7	0.39	10	6, 7, 8, 9, 10, 11
GL 4176	1.2 ± 0.2	1.0/0.2	0.9/0.3	9	<0.5	...	...	...	...	12
Elias 29	6.7 ± 0.5	6.2/0.5	5.2/1.5	32	1.6	0.2/1.4	...	...	...	13, 14
Sgr A*	1.7 ± 0.2	1.7/<0.1	1.0/<0.7	12	<1.5	...	...	...	16.5, 240	15, 16, 17
GCS 3 I	1.1 ± 0.1	1.1/<0.1	0.9/<0.2	4.7	<0.9	...	...	...	...	18
GCS 4	0.7 ± 0.2	0.5/<0.2	0.2/<0.5	3.0	<0.9	...	...	...	...	18
W33 A	14.5 ± 1.3	12.3/2.2	5.1/9.4	90 (470)[e]	8.9	6.6/2.3	5–8	2.8	23, 120	1, 3, 19, 20, 21
GL 2136	7.8 ± 0.3	6.2/1.6	1.9/5.9	50	1.1	1.1/0.	2–4	1.8	17, 580	1, 2, 3, 21, 22
GL 2591	1.6 ± 0.2	1.2/0.4	0.9/0.7	17	<0.2	...	~0.7	1.4	38, 1010	1, 3, 21
S140	4.2 ± 0.1	2.1/2.1	2.0/2.2	21.5	<0.2	...	<2.0	1.4	28, 390	1, 3, 20
NGC 7538 IRS 1	5.1 ± 0.2	4.5/0.6	3.8/1.3	31	1.7	...	...	2.2	25, 176	1, 3
NGC 7538 IRS 9	16.3 ± 1.8	10.8/5.5	9.0/7.3	80	12.	1.4/11.	3–10	1.6	26, 180	1, 2, 3, 19, 21, 23
RAFGL 7009 S	25.0[f]	...	...	110	18.0	...	...	...	...	24

[a] In units of 10^{17} cm^{-2}, unless otherwise specified.
[b] From the best-fitting polar + nonpolar and polar + annealed fits to all features listed in Tables 5 and 6.
[c] Derived from the depth of the silicate stretching feature at 9.7 μm, using the empirical relation $N_H = \tau_{9.7}(3.5 \times 10^{22})$ cm^{-2}.
[d] Asymmetric uncertainty allows for possible systematic error due to high levels of dark current. See Whittet et al. 1998.
[e] Values derived from the 3.1 and 6.0 μm features disagree. See discussions in Allamandola et al. 1992 and Gibb et al. 1999.
[f] An uncertainty of 10% is assumed for trend analyses.

REFERENCES.—(1) Willner et al. 1982; (2) Tielens et al. 1991; (3) Mitchell et al. 1990; (4) Brooke et al. 1996a; (5) Mitchell et al. 1995; (6) Whittet et al. 1998; (7) Whittet et al. 1988; (8) Chiar et al. 1995; (9) Elias 1978a; (10) Pratap et al. 1997; (11) Chiar et al. 1996; (12) Ehrenfreund et al. 1999; (13) Kerr, Adamson, & Whittet 1993; (14) Elias 1978b; (15) McFadzean et al. 1989; (16) Tielens et al. 1996; (17) Serabyn & Güsten 1986; (18) Chiar et al. 1999; (19) Chiar et al. 1998; (20) Allamandola et al. 1992; (21) Whittet & Tielens 1997; (22) Schutte et al. 1996a; (23) Schutte et al. 1996b; (24) d'Hendecourt et al. 1996.

CH_3OH. Perhaps laboratory mixtures containing smaller amounts of CH_3OH may yield similar structures (see Ehrenfreund et al. 1999)

While the spectra of these ices closely resemble those of the polar:nonpolar ices, they contain additional structure that matches the interstellar spectra more closely. Figure 12 displays both sets of fits for the source GL 2136 in all three solid CO_2 IR features.

3.4. *Column Densities*

Column densities of CO_2 (N_{CO_2}), in units of cm^{-2}, were measured using the formula

$$N_{CO_2} = \frac{\int_i \tau(\nu) d\nu}{A_i}, \quad (1)$$

where ν is wavenumber in cm^{-1}, $\tau(\nu)$ is the optical depth spectrum, A_i is the strength of feature i (in units of cm molecule^{-1}), and the integral is taken over the wavenumber range of the feature in question. Where there is sufficient signal-to-noise ratio in both the 4.27 and 15.2 μm features, column densities derived from each individual feature agree to within 24% for each line of sight.

In our data, the differences in N_{CO_2} as derived separately from each of the two CO_2 features are dominated by the uncertainties in the local continuum at 15.2 μm (§ 2.1 and Fig. 5), and are consistent within these error bars. Also, values of N_{CO_2} as derived using the 4.27 μm feature show no consistent deviation from those derived using the 15.2 μm absorption. Thus, within our observational errors, we assume that the 4.27 and 15.2 μm features probe the same CO_2 population. Derived values of N_{CO_2} are listed in Table 7, and their error bars reflect both the uncertainty in the continuum fits as well as the difference between values derived from the 4.27 and 15.2 μm features (where possible). The asymmetric error bars for N_{CO_2} toward Elias 16 allow for possible systematic error in absolute flux level (arising from relatively high levels of dark current in this observation; see discussion in Whittet et al. 1998).

3.4.1. *Correlation of Solid* CO_2 *with Solid* H_2O *and Solid* CO

A strong correlation exists between N_{CO_2} and N_{H_2O} and is shown in Figure 13. All lines of sight observed—including the quiescent cloud medium toward Elias 16—have total CO_2 column densities between 10% and 23% that of H_2O. A weighted fit to all data points passes through the origin to within observational error and indicates that, for an average molecular cloud,

$$\frac{N_{CO_2}}{N_{H_2O}} = 0.17 \pm 0.03 . \quad (2)$$

This value is unaffected (to two significant digits) by the choice of N_{H_2O} for W33 A (see Table 7).

The formation of CO_2 is undoubtedly linked to the CO molecule. A plot of the total column density of CO_2 versus that of CO in the observed lines of sight is shown in Figure 14. The line of sight toward Elias 16 stands out with a relatively high abundance of (nonpolar) CO as a result of its low temperature. It is also apparent from the trend of points in this plot that the correlation line has a positive intercept on the N_{CO_2} axis, implying that significant amounts of CO_2 exist even where there is little or no detectable solid CO. A best fit to the protostars with $N_{CO_2} > 4 \times 10^{17}$ cm^{-2} gives

$$N_{CO_2} = (1.1 \pm 0.1) N_{CO} + (4.2 \pm 0.1) \times 10^{17} \text{ cm}^{-2} . \quad (3)$$

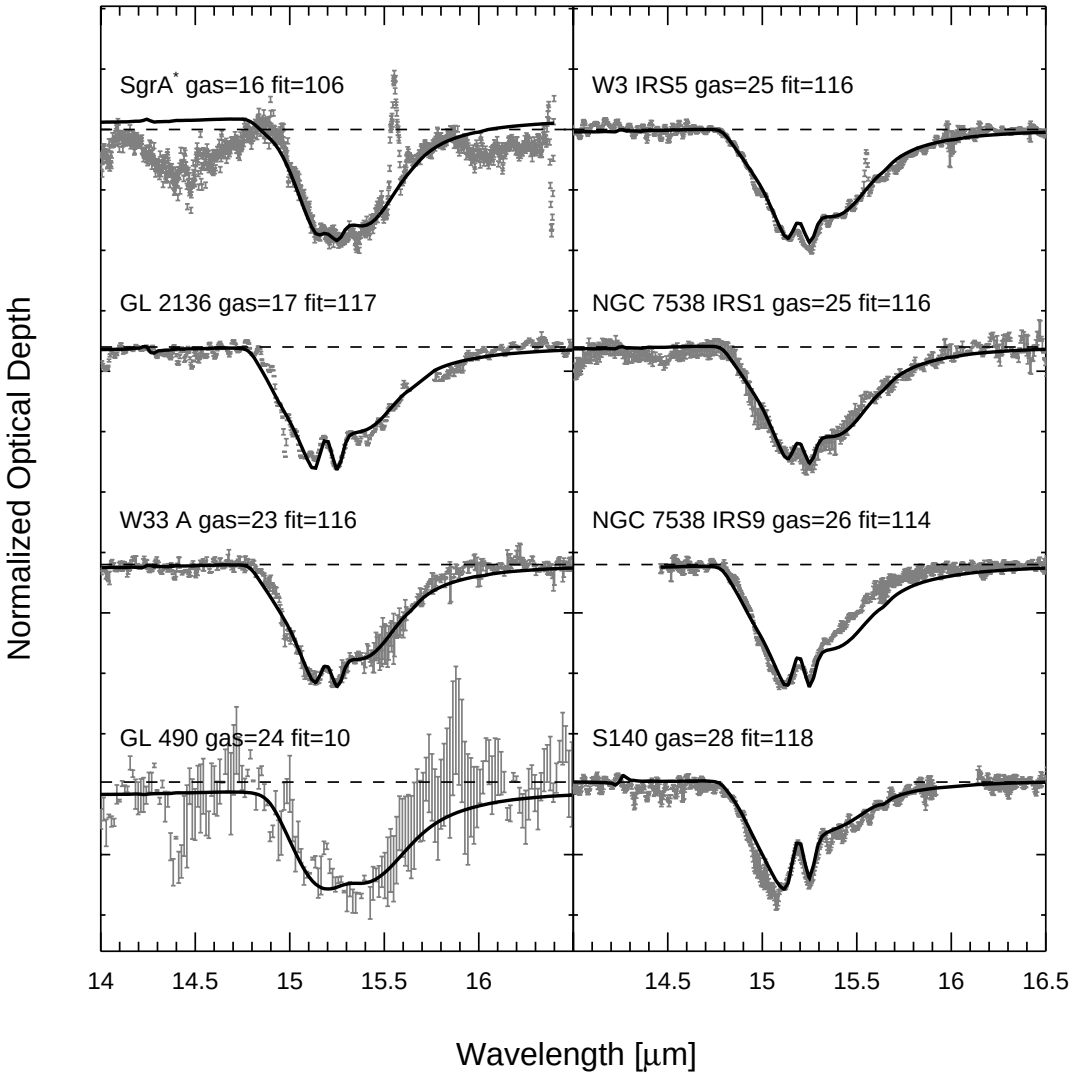

FIG. 11.—Observed solid CO_2 15.2 μm features ordered by cold gas temperature from Table 7 plotted with an $H_2O:CH_3OH:CO_2 = 1:1:1$ mixture at various temperatures. "Fit" refers to the laboratory temperature of the annealed ice whose spectrum is shown.

Since CO is more volatile than CO_2, it will evaporate from the grain surfaces at lower temperatures (sublimation temperatures for pure CO and CO_2 are 17 and 45 K, respectively) and is held within H_2O matrices less effectively than CO_2. CO cannot exist in the more diffuse, outer regions of dark clouds where the interstellar radiation field has a strong influence (Chiar et al. 1995).

Plots of the total and nonpolar solid CO_2 concentrations versus total and nonpolar solid CO concentration in these lines of sight (all relative to H_2O) are shown in Figure 15. No relationship is apparent between the total or nonpolar solid CO_2 phases and the corresponding phases of solid CO. Thus, we obtain no evidence that the formation of CO_2 is linked to the concentration of solid CO in either the polar or nonpolar ice phase.

3.5. *Summary and Conclusions Based on Laboratory Fits*

The observed interstellar solid CO_2 features have been compared to laboratory spectra of two types of ices (§ 3.3): those with separate polar and nonpolar components, and those with separate polar and methanol-rich annealed ice components. The polar + nonpolar laboratory fits are consistent with the hypothesis that the protostellar ISM contains at least two populations of CO_2 ice—one dominated by H_2O, and one by CO_2 itself (or another nonpolar molecule such as CO). The abundance of the nonpolar CO_2 component increases with the line-of-sight gas temperature (Fig. 10). While useful in estimating the relative abundances of polar and nonpolar CO_2, these spectra fail in some cases to reproduce the structure in the solid CO_2 absorption features (see § 3.3.1, Figs. 1, 2, 3, and 4, and Table 5).

The IR profiles of the methanol-rich annealed ices ($H_2O:CH_3OH:CO_2 = 1:1:1$) show a remarkable similarity to the *ISO* spectra (Fig. 11), but observational limits on interstellar solid CH_3OH place its abundance in icy grain mantles well below that of solid CO_2 (Table 7). To test the hypothesis that an underlying component of these spectra is due to an unannealed ice, we performed two-component fits with both unannealed and annealed ice spectra. These fits (see § 3.3.2, Figs. 6, 7, 8, and 9, and Table 6) reproduce much of the structure observed in the solid

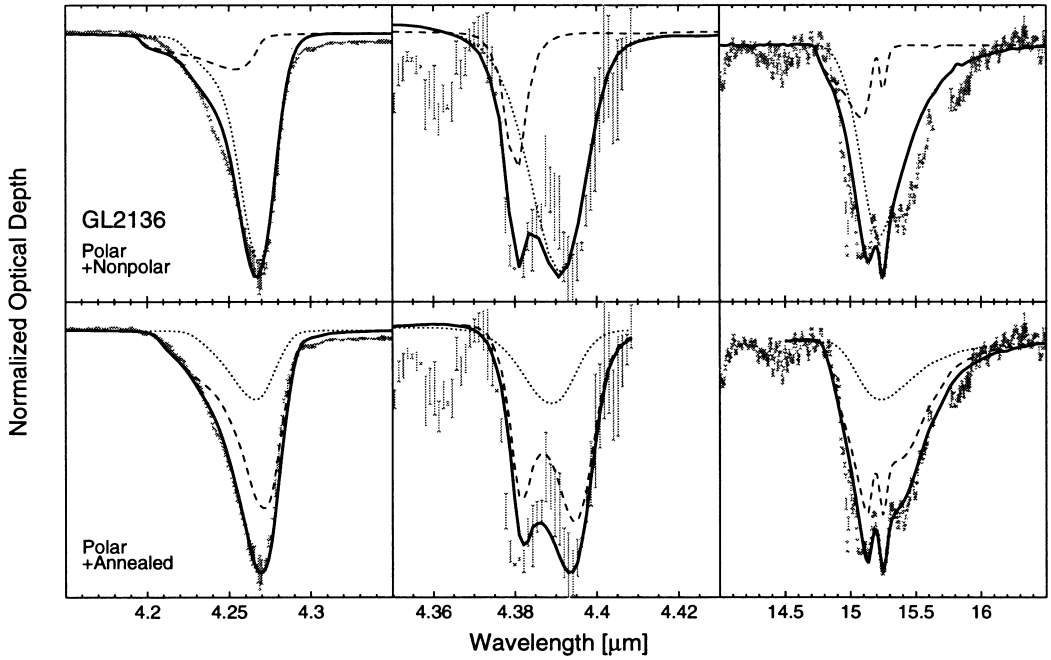

FIG. 12.—Comparison of best overall polar + nonpolar and polar + annealed laboratory fits to the observed solid CO_2 features of GL 2136. The feature of solid $^{13}CO_2$ is shown in the center panels (from Boogert et al. 1999). Dotted lines show polar components of the fits; dashed lines show (*top panels*) nonpolar components and (*bottom panels*) annealed components; and solid lines show sum of fit components.

CO_2 features. Notably, they often reproduce the 15.4 μm shoulder on the solid CO_2 bending mode (unlike the polar + nonpolar fits).

The value of χ_ν^2 has been used in § 3.3 as a estimate of the goodness of a laboratory fit, and Tables 5 and 6 list values of χ_ν^2 for the simultaneous fits to all three solid CO_2 IR features. The overall trend is that the polar + annealed fits give lower χ_ν^2 values (i.e., better agreement) than the polar + nonpolar fits. In general, the fits to individual IR features also give better agreement in the polar + annealed case (NGC 7538 IRS 9 is an exception).

The nature of the best-fitting laboratory mixture may reveal the environment in which the solid CO_2 resides. A polar + nonpolar fit would be appropriate if the CO_2 forms in each type of ice mantle. In contrast, the polar + annealed fits represent ices where CO_2 is formed entirely in the polar phase, later segregating when heated into components of H_2O:CO_2, CH_3OH:CO_2, and pure CO_2.

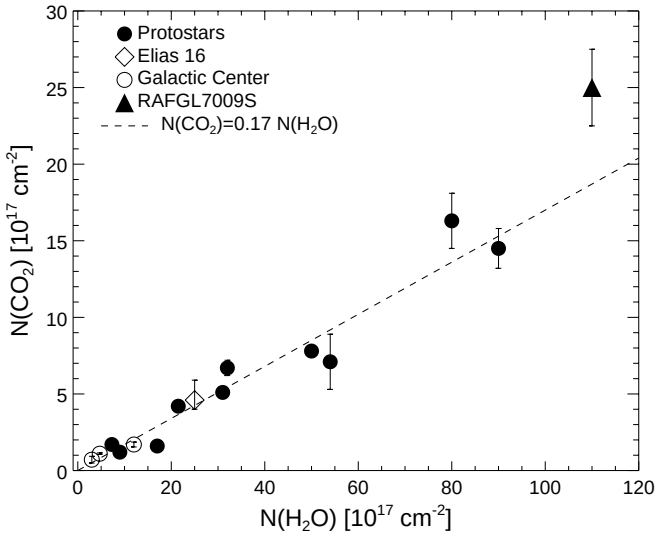

FIG. 13.—Solid CO_2 column density vs. that of solid H_2O toward sources in Table 7. Squares show Galactic Center sources; circles show protostars; diamond shows Elias 16 (quiescent cloud); triangle– RAFGL 7009 S (d'Hendecourt et al. 1996; 10% uncertainty assumed); the dashed line indicates the average of all data, $N_{CO_2} = 0.17 N_{H_2O}$.

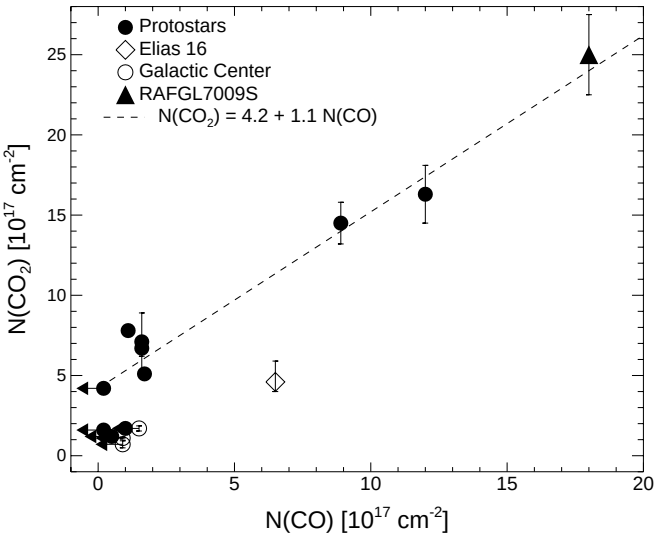

FIG. 14.—Total solid CO_2 column density vs. total solid CO column density in the observed lines of sight. Symbols are as in Fig. 13. Arrows indicate upper limits on N_{CO}. The dashed line indicates the trend for protostars with $N_{CO_2} > 4 \times 10^{17}$ cm^{-2}: $N_{CO_2} = 4.2 \times 10^{17}$ cm^{-2} + $1.1 N_{CO}$.

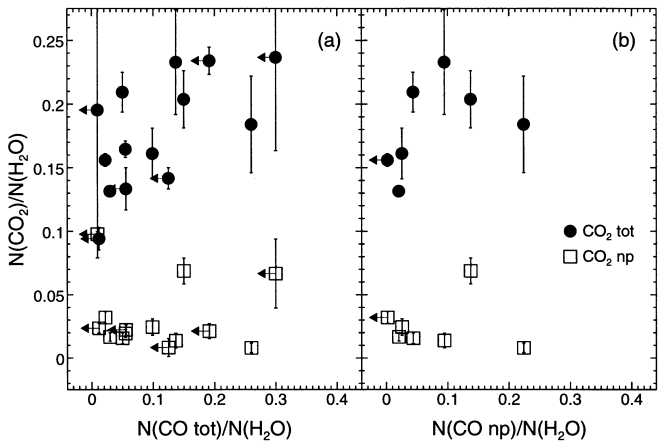

FIG. 15.—Column densities, normalized to solid H_2O, of total and nonpolar solid CO_2 vs. (*a*) total and (*b*) nonpolar solid CO. Filled circles show total CO_2; squares show nonpolar CO_2. Arrows indicate upper limits on solid CO.

The latter picture is consistent with these observations —the solid CO_2 toward Elias 16 (a known quiescent cloud source) seems to be contained entirely (>95%) within the polar phase, and increasing abundances of nonpolar (or annealed) CO_2 exist toward warm protostellar regions.

4. DISCUSSION

4.1. *Protostars versus Field Stars: Evidence for Thermal Processing*

In general, three processes are thought to play important roles in the formation and evolution of ice mantles: (1) grain surface reactions, (2) processing by UV photolysis or particle bombardment, and (3) thermal processing leading to sublimation, segregation and/or annealing. Of these, process 1 must be the dominant source of primary ices in molecular clouds, as there is simply no other way to explain the abundance of H_2O, the dominant constituent, in the mantles (e.g., Whittet 1992). Process 2 is often assumed to play the key role in regions of recent star formation, driving the evolution of the ices from simple volatiles to more complex organic refractory materials (Agarwal et al. 1985). Detection of ubiquitous solid CO_2 might seem consistent with this assumption, given the ease with which CO_2 is formed by photolysis reactions in laboratory ices. However, our detailed analysis of the observations (§ 3) lead us to conclude that it is thermal processing irradiation rather than by UV and/or cosmic rays that is the dominant process in molecular clouds close to young stars.

As already discussed, the sources in our sample fall essentially into two broad groups, "field stars," in which there is little or no interaction between the source and the molecular cloud containing the CO_2, and "embedded protostars," in which the surrounding molecular cloud may be heated and/or irradiated by the source itself. The prototypical field star is Elias 16. Although we do not know the exact location of the molecular clouds toward the Galactic Center, it is reasonable to place Sgr A*, at least, in a group with Elias 16.

The area of sky included in the SWS aperture centered on Sgr A* is about 14″ × 20″–27″ (wavelength dependent), so the observed spectrum likely includes flux contributions from several Galactic Center infrared sources (GC IRS 1, 2, 3, 6, 7, 9, 10, and 21). In common with Elias 16, molecular cloud material toward Sgr A* appears to be cold, with CO_2 residing almost entirely in polar ice matrices: the 15.2 μm feature lacks structure associated with annealing; although the 15.2 μm feature of Elias 16 is unavailable for direct comparison (because of this star's low flux level and the SWS sensitivity at that wavelength), fits to its stretching mode preclude a strong nonpolar contribution (Whittet et al. 1998). Detection of solid CO in the spectra of some of the individual IR sources toward Sgr A* (McFadzean et al. 1989; Chiar et al. 1999) is further evidence that the molecular cloud(s) in this general line of sight is (are) cold. Serabyn & Güsten (1986) measured the kinetic temperature of NH_3 gas toward Sgr A* and found two components with temperatures of 16.5 ± 2.5 K and 240 ± 100 K, consistent with values based on CO observations by Hüttemeister et al. (1993) of ~25 and 200 K. We therefore assume that the icy material is associated with gas at ~15–25 K.

Our results show that CO_2 toward protostellar sources is an indicator of thermal annealing in each line of sight, and its matrix interactions trace the thermal history of the ices present with a high degree of sensitivity. Especially sensitive is the splitting of the bending mode in molecular complexes and when the axial symmetry of the molecule is broken. Toward sources previously thought to have the highest levels of processing (W33 A, GL 2136), a strong shoulder at 15.4 μm, due the formation of molecular complexes with CH_3OH and other polar molecules (Ehrenfreund et al. 1999), appears.

The consistency in CO_2/H_2O ratio from source to source (Fig. 13) implies that the CO_2 column density does not depend on the irradiation dose due to the protostellar UV flux but merely on the amount of total molecular material present. If CO_2 is formed by reactions of H_2O and CO, then a correlation between the abundances of solid CO_2 and CO should exist (in either the polar or nonpolar ice phase), but no clear evidence is present in the observed column densities (Fig. 15). The correlations seem to reflect merely the temperature dependences of the CO_2 polar and nonpolar phases (Fig. 10).

If CO_2 is formed by $CO + O \rightarrow CO_2$ on grain surfaces, the limiting factor may be the abundance of atomic O, which quickly becomes devoured in the formation of both CO and O_2 (Chiar 1997). Perhaps the concentration of CO_2 observed is the end result of a photochemical equilibrium between different mantle constituents. However, field stars provide the control group for the results on protostars: the fact that the CO_2/H_2O ratio in Elias 16 and Sgr A* is comparable with that for the protostellar sources (Fig. 13) implies that CO_2 is formed in the absence of embedded sources, and thus before any processing by UV photons takes place (other than that induced by cosmic rays and the weak interstellar radiation field within dense clouds). The primary conclusion of our study is thus simply that *the spectral evolution of the* CO_2*-bearing ices is dominated by thermal processing.*

4.2. *Thermal Annealing and the Evolution of the Ices*

Although evidence for thermal processing is found in our observations, it seems unlikely that this process is implicated in the formation of CO_2. The presence of CO_2 in field stars indicates that it must form at low temperature, by surface reactions or by processing driven by cosmic rays or the interstellar radiation field (see Whittet et al. 1998 for

further discussion). In any case, the consistent CO_2/H_2O ratio from source to source implies a formation process for CO_2 that is the same in all clouds (e.g., a similar cosmic-ray ionization rate, if the formation is by cosmic-ray–induced UV). This question is yet to be resolved.

The simple overall picture we may draw from our observations is that CO_2 is formed in an H_2O-rich environment at an abundance of 17% relative to H_2O ice *in the quiescent cloud environment*. Likely, some methanol is formed in this ice as well. Subsequent warm-up of this ice by a newly formed star leads to the formation of $CH_3OH:CO_2$ complexes and eventually complete ice segregation into H_2O-rich and CO_2-rich ice phases *on the same grain*. The same heating leads to the evaporation of any nonpolar CO ice mantle present.

Finally, we consider the (perhaps) surprising lack of evidence for radiative processing by embedded protostars in our data. Observations of compact H II regions (Chini et al. 1986a, 1986b; Wood, Churchwell, & Salter 1988; Wood & Churchwell 1989) require the presence of OB stars in order to explain IR flux levels emitted from the dust that encloses them. These regions are likely to be radiation limited; i.e., their boundaries are determined by the flux of photons beyond the Lyman limit rather than by the availability of material to be ionized. The radiation that escapes the H II and photon-dominated regions has an energy below that required for the ionization of H (13.6 eV) and the dissociation of H_2 and CO (11.3–13.6 eV). The UV radiation field is lowered only by dust extinction beyond the photon-dominated region. However, the general absence of recombination lines in the spectra of our observed sources suggests that many have not yet reached the stage of forming extended H II regions, and therefore UV processing by the embedded protostars may play only minor roles in the evolution of the CO_2-bearing ices. Thermal processing, on the other hand, may be driven by copious IR radiation from young stars, which is ubiquitous and relatively unattenuated. For instance, a previous study of the methanol C–O stretch toward GL 2136 by Skinner et al. (1992) has shown that thermal segregation of the $H_2O:CH_3OH$ ices plays an important role there.

We are indebted to the SRON-MPE SWS teams and the SIDT. P. A. G. and D. C. B. W. are supported by NASA grants NAG 5-3339 and NAG 5-7410. P. E. is a recipient of an APART fellowship of the Austrian Academy of Sciences. The *ISO* research of E. F. v. D. and W. A. S. is supported by ASTRON, SRON, and NFRA grant 781-76-015. J. E. C. holds a National Research Council-ARC Research Associateship. This research has made use of the Leiden Observatory Laboratory database of spectra.[10] This work was supported by NASA through JPL contract 961624 and NASA grants NAG5-7410 and NAG5-7598.

[10] The Leiden Observatory Laboratory database of spectra is available on the World Wide Web at http://www.strw.leidenuniv.nl/~lab/.

REFERENCES

Agarwal, V. K., et al. 1985, Origins Life Evol. Biosphere, 16, 21
Allamandola, L. J., Sandford, S. A., Tielens, A. G. G. M., & Herbst, T. M. 1992, ApJ, 399, 134
Boogert, A. C. A., Ehrenfreund, P., Gerakines, P. A., Tielens, A. G. G. M., Whittet, D. C. B., Schutte, W. A., van Dishoeck, E. F., & de Graauw, Th. 1999, A&A, in press
Boogert, A. C. A., Helmich, F. P., van Dishoeck, E. F., Schutte, W. A., Tielens, A. G. G. M., & Whittet, D. C. B. 1998, A&A, 336, 352
Boogert, A. C. A., et al. 1996, A&A, 315, L377
Boonman, A., et al. 1999, in preparation
Brooke, T. Y., Sellgren, K., & Smith, R. G. 1996a, ApJ, 459, 209
Brooke, T. Y., Tokunaga, A. T., Weaver, H. A., Crovisier, J., Bockelee-Morvan, D., & Crisp, D. 1996b, Nature, 383, 606
Chiar, J. E. 1997, Origins Life Evol. Biosphere, 27, 79
Chiar, J. E., Adamson, A. J., Kerr, T. H., & Whittet, D. C. B. 1994, ApJ, 426, 240
———. 1995, ApJ, 455, 234
Chiar, J. E., Adamson, A. J., & Whittet, D. C. B. 1996, ApJ, 472, 665
Chiar, J. E., Gerakines, P. A., Whittet, D. C. B., Pendleton, Y. J., Tielens, A. G. G. M., Adamson, A. J., & Boogert, A. C. A. 1998, ApJ, 498, 716
Chiar, J. E., et al. 1999, in preparation
Chini, R., Kreysa, E., Mezger, P. G., & Gemünd, H.-P. 1986a, A&A, 154, L8
———. 1986b, A&A, 157, L1
de Graauw, Th., et al. 1996a, A&A, 315, L49
———. 1996b, A&A, 315, L345
d'Hendecourt, L. B., Allamandola, L. J., & Greenberg, J. M. 1985, A&A, 152, 130
d'Hendecourt, L., et al. 1996, A&A, 315, L365
Ehrenfreund, P., Boogert, A. C. A., Gerakines, P. A., Jansen, D. J., Schutte, W. A., Tielens, A. G. G. M., & van Dishoeck, E. F. 1996, A&A, 315, L341
Ehrenfreund, P., Boogert, A. C. A., Gerakines, P. A., Tielens, A. G. G. M., & van Dishoeck, E. F. 1997, A&A, 328, 649
Ehrenfreund, P., et al. 1999, in preparation
Elias, J. H. 1978a, ApJ, 224, 453
———. 1978b, ApJ, 224, 857
Gerakines, P. A., Schutte, W. A., Greenberg, J. M., & van Dishoeck, E. F. 1995, A&A, 296, 810
Gibb, E., et al. 1999, in preparation
Grim, R. J. A., Baas, F., Greenberg, J. M., Geballe, T. R., & Schutte, W. A. 1991, A&A, 243, 473
Grim, R. J. A., & d'Hendecourt, L. B. 1986, A&A, 167, 161
Gürtler, J., Henning, T., Koempe, C., Pfau, W., Krätschmer, W., & Lemke, D. 1996, A&A, 315, L189
Hasegawa, T. I., & Herbst, E. 1993, MNRAS, 263, 589
Herbst, E., & Leung, C. M. 1989, ApJS, 69, 271
Hüttemeister, S., Wilson, T. L., Bania, T. M., & Martín-Pintado, J. 1993, A&A, 280, 255
Kerr, T. H., Adamson, A. J., & Whittet, D. C. B. 1993, MNRAS, 262, 1047
Lacy, J. H., Baas, F., Allamandola, L. J., Persson, S. E., McGregor, P. J., Lonsdale, C. J., Geballe, T. R., & van de Bult, C. E. P. 1984, ApJ, 276, 533
Lutz, D., et al. 1996, A&A, 315, L269
McFadzean, A. D., Whittet, D. C. B., Bode, M. F., Adamson, A. J., & Longmore, A. J. 1989, MNRAS, 241, 873
Millar, T. J., Bennett, A., Rawlings, J. M. C., Brown, P. D., & Charnley, S. B. 1991, A&AS, 87, 585
Mitchell, G. F., Lee, S. W., Maillard, J.-P., Matthews, H., Hasegawa, T. I., & Harris, A. I. 1995, ApJ, 438, 794
Mitchell, G. F., Maillard, J.-P., Allen, M., Beer, R., & Belcourt, K. 1990, ApJ, 363, 554
Moore, M. H., Khanna, R., & Donn, B. 1991, J. Geophys. Res., 96, 17,541
Pratap, P., Dickens, J. E., Snell, R. L., Miralles, M. P., Bergin, E. A., Irvine, W. M., & Schloerb, F. P. 1997, ApJ, 486, 862
Sandford, S. A., & Allamandola, L. J. 1990, ApJ, 355, 357
Savage, B. D., Bohlin, R. C., Drake, J. F., & Budich, W. 1977, ApJ, 216, 291
Schaeidt, S. G., et al. 1996, A&A, 315, L55
Schutte, W. A., Gerakines, P. A., Geballe, T. R., van Dishoeck, E. F., & Greenberg, J. M. 1996a, A&A, 309, 633
Schutte, W. A., & Greenberg, J. M. 1997, A&A, 317, L43
Schutte, W. A., Tielens, A. G. G. M., & Sandford, S. A. 1991, ApJ, 382, 523
Schutte, W. A., et al. 1996b, A&A, 315, L333
Serabyn, E., & Güsten, R. 1986, A&A, 161, 334
Shalabiea, O. M., & Greenberg, J. M. 1994, A&A, 290, 266
Skinner, C. J., Tielens, A. G. G. M., Barlow, M. J., & Justtanont, K. 1992, ApJ, 399, L79
Snyder, L. E. 1997, Origins Life Evol. Biosphere, 27, 115
Tegler, S. C., Weintraub, D. A., Rettig, T. W., Pendleton, Y. J., Whittet, D. C. B., & Kulesa, C. A. 1995, ApJ, 439, 279
Tielens, A. G. G. M., & Allamandola, L. J. 1987, in Interstellar Processes, ed. D. Hollenbach & H. Thronson (Dordrecht: Reidel), 397
Tielens, A. G. G. M., & Hagen, W. 1982, A&A, 114, 245
Tielens, A. G. G. M., Tokunaga, A. T., Geballe, T. R., & Baas, F. 1991, ApJ, 381, 181
Tielens, A. G. G. M., & Whittet, D. C. B. 1997, in IAU Symp. 178, Molecules in Astrophysics: Probes and Processes, ed. E. F. van Dishoeck (Dordrecht: Kluwer), 45
Tielens, A. G. G. M., Wooden, D. H., Allamandola, L. J., Bregman, J., & Witteborn, F. C. 1996, ApJ, 461, 210
Trotta, F. 1996, Ph.D. thesis, LGGE-CNRS, Université Joseph Fourier

Valentijn, E. A., et al. 1996, A&A, 315, L60
van Dishoeck, E. F., & Blake, G. A. 1998, ARA&A, 36, 317
van Dishoeck, E. F., et al. 1996, A&A, 315, L349
Whittet, D. C. B. 1992, Dust in the Galactic Environment (New York: IOP)
Whittet, D. C. B., Bode, M. F., Longmore, A. J., Adamson, A. J., McFadzean, A. D., Aitken, D. K., & Roche, P. F. 1988, MNRAS, 233, 321
Whittet, D. C. B., & Tielens, A. G. G. M. 1997, in ASP Conf. Ser. 122, From Stardust to Planetesimals, ed. Y. J. Pendleton & A. G. G. M. Tielens (San Francisco: ASP), 161
Whittet, D. C. B., et al. 1996, A&A, 315, L357
———. 1998, ApJ, 498, L159
Willner, S. P., et al. 1982, ApJ, 253, 174
Wood, D. O. S., & Churchwell, E. 1989, ApJS, 69, 831
Wood, D. O. S., Churchwell, E., & Salter, C. J. 1988, ApJ, 325, 694

THE ASTROPHYSICAL JOURNAL, 526:1062, 1999 December 1

ERRATUM

The title of the paper by P. A. Gerakines et al. (ApJ, 522, 357 [1999]) was typeset incorrectly as the result of an error at the University of Chicago Press. The correct title should read "Observations of Solid Carbon Dioxide in Molecular Clouds with the *Infrared Space Observatory*." The Press apologizes for this error.